Olfactory-driven beta band entrainment of limbic circuitry during neonatal development

Johanna K. Kostka & Ileana L. Hanganu-Opatz

Institute of Developmental Neurophysiology, Center for Molecular Neurobiology, University Medical Center Hamburg-Eppendorf, 20251 Hamburg, Germany

Corresponding authors: Ileana L. Hanganu-Opatz
hangop@zmnh.uni-hamburg.de

Johanna K. Kostka
johanna.kostka@zmnh.uni-hamburg.de

Figures: 6
Supplementary Material: 5 figures, 12 tables
Number of pages: 35

Number of words in Abstract: 156
Number of words in Introduction: 670
Number of words in Discussion: 1220

ABSTRACT

Cognitive processing relies on the functional refinement of the limbic circuitry during the first two weeks of life. During this developmental period, when most sensory systems are still immature, the sense of olfaction acts as "door to the world", providing the main source of environmental inputs. However, it is unknown whether early olfactory processing shapes the development of the limbic circuitry. Here, we address this question by combining simultaneous *in vivo* recordings from the olfactory bulb (OB), lateral entorhinal cortex (LEC), hippocampus (HP), and prefrontal cortex (PFC) with opto- and chemogenetic manipulations of mitral/tufted cells (M/TCs) in the OB of non-anesthetized neonatal mice. We show that the neonatal OB synchronizes the limbic circuity in beta frequency range. Moreover, it drives neuronal and network activity in LEC, as well as subsequently, HP and PFC via long-range projections from mitral cells (MCs) to HP-projecting LEC neurons. Thus, OB activity controls the communications within limbic circuits during neonatal development.

1 **INTRODUCTION**

2 Coordinated neuronal activity during early development refines the neural circuits that account
3 for complex processing in the adult brain. During the first two postnatal weeks, when rodents
4 are still blind, deaf, and perform no active whisking, coordinated activity patterns in the sensory
5 periphery occur independently of sensory input (Hanganu-Opatz, 2010; Leighton and
6 Lohmann, 2016). Spontaneous neuronal discharges in the retina, cochlea, and whisker pad
7 trigger discontinuous oscillatory bursts in the corresponding primary sensory cortices (Ackman
8 et al., 2012; Hanganu et al., 2006; Khazipov et al., 2004; Mizuno et al., 2014; Wang and
9 Bergles, 2015) that are necessary for the development of sensory discrimination (Che et al.,
10 2018). Similar activity patterns can also be observed in brain areas involved in higher cognitive
11 processing. Discontinuous theta band oscillations in the LEC entrain similar activity patterns in
12 the HP, which in turn entrains the prelimbic area (PL) of the PFC (Ahlbeck et al., 2018;
13 Bitzenhofer et al., 2017b; Brockmann et al., 2011; Hartung et al., 2016a). Disturbance of these
14 early activity patterns in mouse models of psychiatric risk (Chini et al., 2020; Domnick et al.,
15 2015; Hartung et al., 2016b; Richter et al., 2019; Xu et al., 2021) as well as through
16 pharmacological (Krüger et al., 2012) or optogenetic manipulations (Bitzenhofer et al., 2021)
17 led to disruption of adult circuits and behavioral abilities. However, it is not clear whether
18 stimulus-independent activity patterns in the sensory periphery impact the development of
19 limbic networks.

20 Due to the limited or absent functionality of most sensory systems during the first two
21 postnatal weeks, their contribution to the development of limbic networks has been considered
22 negligible. This hypothesis has been supported by data showing that the synchrony between
23 V1 and the HP-PFC network before eye-opening is rather weak (Brockmann et al., 2011). In
24 contrast to other sensory systems, the olfactory system is functional early in life and newborn
25 mice heavily depend on it for survival (Logan et al., 2012). Correspondingly, the anatomical
26 pathways from OB to cortical areas are unique among sensory systems. MCs send afferents
27 to the piriform cortex (PiR) and limbic brain areas such as LEC and amygdala, lacking the relay
28 through the thalamus (Igarashi et al., 2012; Luskin and Price, 1983). At adult age, in line with
29 the anatomical connectivity, strong functional coupling during odor processing has been found
30 between OB and these brain areas. For example, adult olfactory processing relies on
31 respiration-modulated beta and gamma OB activity (Kay, 2014; Neville and Haberly, 2003).
32 Further, beta oscillations in PiR, LEC, and HP play a critical role in olfactory memory
33 processing (Gourévitch et al., 2010; Vanderwolf and Zibrowski, 2001; Xu and Wilson, 2012).
34 Moreover, synchronized beta oscillations between OB-HP and LEC-HP are critically involved
35 in odor learning (Igarashi et al., 2014; Martin et al., 2007, 2006; Ravel et al., 2003). Recently,
36 beta oscillations in prefrontal-hippocampal networks have been identified to support the
37 utilization of odor cues for memory-guided decision making (Symanski et al., 2021).

38   The tight and behaviorally relevant coupling between OB and limbic circuits at adult age
39   leads to the question, which role does olfactory activation early in life play for these circuits.
40   Previously, we showed that discontinuous oscillatory activity in the theta-beta range, emerging
41   as a result of bursting MCs in the neonatal OB, entrains similar oscillatory patterns in LEC
42   (Gretenkord et al., 2019; Kostka et al., 2020). However, the role of neuronal and network
43   activity in the OB for the functional development of downstream areas within limbic circuits is
44   still largely unknown.

45   To address this knowledge gap, we simultaneously monitored single-unit activity (SUA)
46   and local field potentials (LFP) in OB, LEC, HP, and PFC of non-anesthetized neonatal mice
47   (postnatal day (P) 8-10) during manipulation of M/TC activity using excitatory opsins and
48   inhibitory DREADDs. We show that activation of M/TCs triggers action potential firing in LEC
49   and HP as well as prominent beta oscillations that synchronize the OB with the downstream
50   cortical areas. These data document the ability of coordinated activity at the sensory periphery
51   to shape the development of circuits accounting for cognitive processing.

52

53   **RESULTS**

54   **Oscillatory activity in OB times the network activity in limbic circuits of neonatal mice**

55   To get first insights into the impact of OB activity on developing cortical circuits including LEC,
56   HP, and PFC, we simultaneously recorded the LFP and multiunit activity (MUA) in all four brain
57   areas in non-anesthetized neonatal (P8-10) mice (n=56, Figure 1A, B) and assessed the
58   temporal relationships between network oscillations and neuronal firing. All investigated areas
59   showed discontinuous oscillatory activity in theta-beta range (Brockmann et al., 2011;
60   Gretenkord et al., 2019; Hartung et al., 2016a), accompanied by continuous low amplitude slow
61   frequency oscillations peaking at 2-4 Hz (respiration rhythm, RR) (Figure 1B). Half (med:
62   53.779 %, iqr: 47.681 – 65.104 %, n=20) of the oscillatory events detected in OB co-occurred
63   in all four brain regions. To quantify the coupling of OB to cortical areas, we calculated the
64   imaginary coherence (Figure 1C). While a high level of synchrony linked OB with all
65   investigated cortical areas, the strength of coupling was frequency-dependent, having the
66   highest magnitude in the beta frequency range for OB-LEC and OB-HP and in the RR
67   frequency band for OB-LEC and OB-PFC.

68   To uncover whether OB activity times the neuronal firing of cortical areas, we calculated
69   the phase-locking of single units (SUA) recorded in OB, LEC, HP, and PFC to beta band
70   oscillations (12-30 Hz) in OB (Figure 1D). Significantly locked OB units fired shortly before the
71   trough of the beta cycle, while LEC and HP units were locked to significantly shifted phase
72   angles (Figure 1D, Table S1, 2). Solely the prefrontal firing showed no phase preference of
73   locking to the oscillatory phase in OB. Next, we questioned whether the communication

74   between OB and cortical areas is directed and whether OB acts as a driving force within the
75   circuit. For this, we assessed the temporal relationship between the firing in cortical regions
76   and OB by calculating the standardized cross-covariance of unit pairs (Siapas et al., 2005).
77   For unit pairs between OB and LEC, OB and HP, and OB and PFC, the peak of cross-
78   covariance was at negative time-lags, indicating that spiking in OB preceded cortical firing
79   (Figure 1E). Monitoring the timing of interactions between cortical areas (LEC-HP, LEC-PFC,
80   and HP-PFC) confirmed the previously reported directionality of communication (Hartung et
81   al., 2016a), yet less clear as for the OB-driven coupling. As spike-dependent methods are
82   strongly biased by the firing rate of investigated neurons, which is rather low in neonatal mice,
83   we next used the spectral dependency ratio (SDR), a method that infers causal direction from
84   time-series data (Ramirez-Villegas et al., 2021; Shajarisales et al., 2015), to confirm the
85   directed communication between OB and cortical areas. SDR values for OB → LEC were
86   significantly higher than for LEC → OB, supporting the drive from OB to LEC. Further, the SDR
87   analysis revealed a spectral dependency of HP as well as PFC on OB, suggesting the
88   contribution of OB activity to the oscillatory entrainment of prefrontal and hippocampal circuits
89   (Figure 1F, Table S3). Moreover, the analysis confirmed the previously reported directed
90   interaction from HP to PFC and LEC to PFC (Brockmann et al., 2011; Hartung et al., 2016a).
91   No SDR difference was detected for LEC-HP, indicating that, in line with anatomical data
92   (Hartung et al., 2016a), a bidirectional coupling links HP and LEC (Figure 1F, Table S3).

93   Thus, tight directed interactions between OB and cortical areas ensure timed firing and
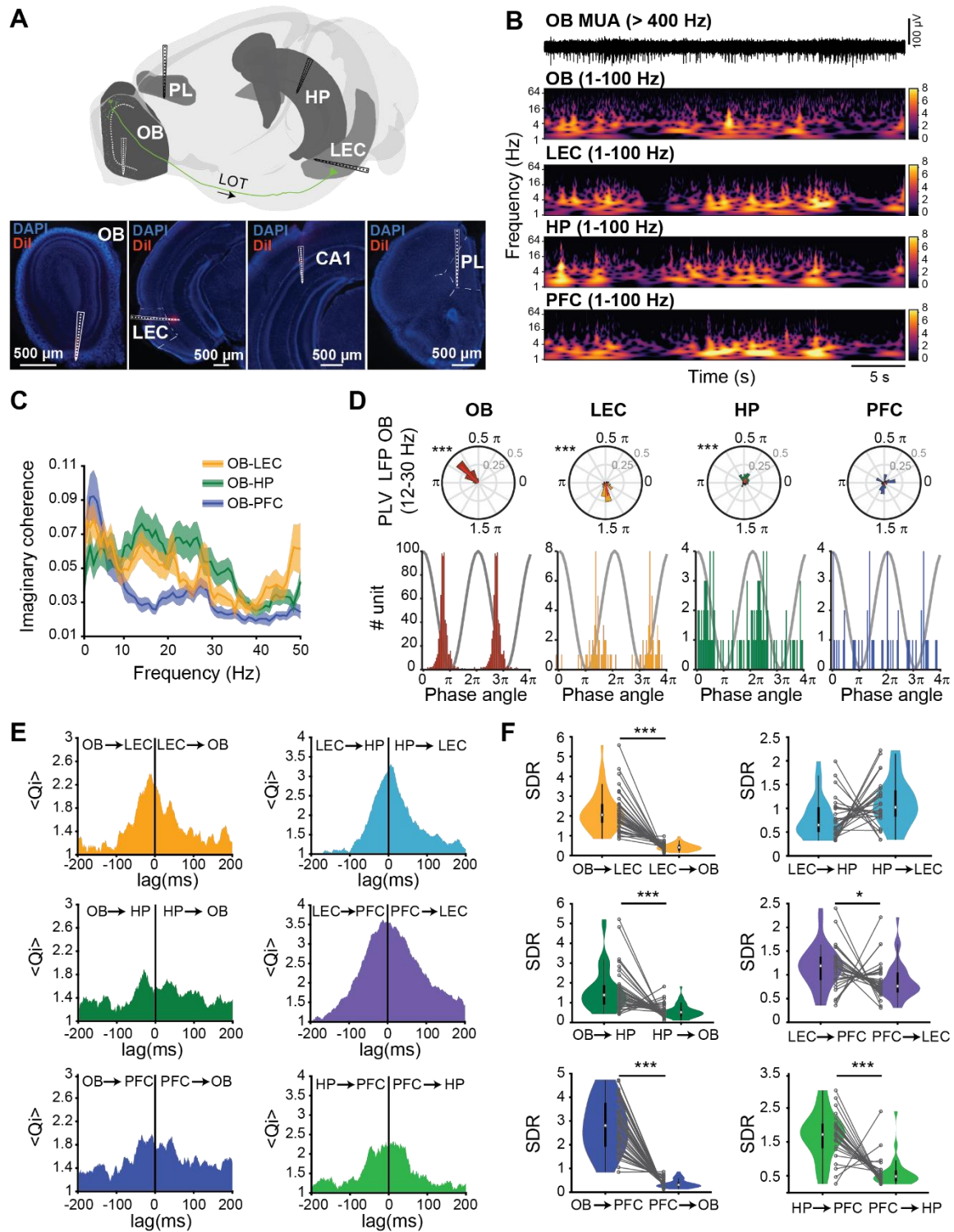94   oscillatory entrainment within downstream LEC-HP circuits.

Figure 1: Functional coupling between neonatal OB, LEC, HP, and PFC

Figure 1: Functional coupling between neonatal OB, LEC, HP, and PFC

A. Top, schematic of recording configuration for simultaneous extracellular recordings in OB, LEC, HP, and PFC. The positions of recording sites were displayed superimposed on the corresponding brain areas (Brainrender, Claudi et al., 2020). Bottom, digital photomontages displaying the DiI-labeled (red) electrode tracks in DAPI (blue) stained slices of OB, LEC, HP, and PL of a P10 mouse.

B. Representative MUA trace recorded in the mitral cell layer (MCL) displayed together with the wavelet spectra of LFP recorded simultaneously in OB, LEC, HP, and PFC.

C. Spectra of imaginary coherence calculated for OB - LEC (yellow), OB - HP (green), and OB - PFC (blue).

D. Top, polar plots displaying the phase-locking of significantly locked units in OB (red), LEC (yellow), HP (green), and PFC (blue) to beta oscillations in OB. Bottom, histograms of mean phase angle for significantly phase-locked OB (red), LEC (yellow), HP (green), and PFC (blue) units. Histograms are replicated over two OB beta cycles (gray curve). (Rayleigh test for non-uniformity, *** $p < 0.001$)

E. Plots of standardized mean spike-spike cross-covariance for OB - LEC (yellow), OB - HP (green), OB - PFC (blue), LEC - HP (light blue), LEC - PFC (purple), and HP - LEC (light green). Negative lags indicate that spiking in the first brain area precedes spiking in the second brain area.

F. Spectral dependency ratio (SDR) calculated for OB - LEC (yellow), OB - HP (green), OB - PFC (blue), LEC - HP (light blue), LEC - PFC (purple), and HP - LEC (light green). Gray dots and lines correspond to individual animals. (* $p < 0.05$, ** $p < 0.01$, *** $p < 0.001$, Wilcoxon signed-rank test).

## Activation of M/TCs induces beta oscillations in neonatal OB

To elucidate the mechanisms of directed communication between OB and downstream cortical areas, we activated ChR2-transfected M/TCs by light and simultaneously monitored the network and neuronal activity in neonatal LEC, HP, and PFC. Transfection of M/TCs was achieved using a cre-dependent virus vector (AAV9-Ef1a-DIO-hChR2(E123T/T159C)-EYFP) that was injected into the right OB of P1 Tbet-cre mice (Figure 2A). ChR2-EYFP expression was reliably detected in M/TCs and their projections 7 days after injection (Figure 2B). Ramp light stimuli of increasing intensity (473 nm, total duration 3 s) were used to activate M/TCs in the OB of P8-10 mice (Figure 2A). The stimulation parameters have been set in line with previous data (Bitzenhofer et al., 2017a) to prevent not only firing as a result of tissue heating but also artificially synchronous firing patterns and large stimulation artifacts. Ramp stimulation led to a sustained increase of spike discharge and broad-band (4-100 Hz) LFP power augmentation in OB that peaked in beta frequency range (12-30 Hz) (Figure 2C, D, S1A). In cre+ mice, the modulation indices (MI) for theta, beta, and gamma power were significantly increased and different from those calculated for cre- animals (Figure 2Dii, Table S5). Correspondingly, SUA strongly augmented during ramp stimulation (Figure 2E, F). This activation was not layer-specific and, mirroring the tight OB wiring, not only M/TCs but also granule cells (GCs) and other OB interneurons increased their firing in response to light activation of ChR2-transfected M/TCs (Figure S1B, C). Analysis of the firing onset along OB layers confirmed the global activation. Cells in the MCL and GCL started to fire immediately

115   after the 3 ms-long light pulses, whereas cells in the extra plexiform layer (EPL) and glomerular

116   layer (GL) responded with a brief delay (Figure 2G).

117   To assess the temporal relationship between neuronal firing and beta oscillations in

118   OB, we calculated the locking of SUA firing to the oscillatory phase before (Pre) and during

119   (Stim) light stimulation. Ramp stimulation caused a significantly stronger locking of OB units to

120   beta oscillations (Pre: med: 0.147, iqr: 0.094 – 0.227; Stim: med: 0.180, iqr: 0.103 – 0.294,

121   n_{units}=176 from 26 mice, p=9.39*10^{-5}, LMEM) (Figure 2Hi) and an augmentation of the

122   proportion of significantly phase-locked units to the beta rhythm during ramp stimulation (Pre:

123   16.478 %, 29/176 units, Stim: 55.114 %, 97/176 units, p=3.12*10^{-14}, Fisher's exact test) (Figure

124   2Hii). Of note, the coupling of OB units to the RR phase was weaker (Pre: med: 0.129, iqr:

125   0.080 – 0.220, Stim: med: 0.097, iqr: 0.057 – 0.157, n_{units}=176 from 26 mice, p=7.782*10^{-6},

126   LMEM) (Figure S1D) even though the proportion of locked units (Pre: 14.773 %, 26/176 units,

127   Stim: 14.205 %, 25/176 units, p=1, Fisher's exact test) and the power of RR oscillations were

128   not altered upon light stimulation (Figure S1D(iii), 2D). In contrast, light stimulation had no

129   effects on the phase-locking of OB units to oscillatory phase in cre^{-} mice (Figure S1E, Table

130   S4). The larger beta power observed during ramp stimulation might result from increased M/TC

131   and interneuronal firing, since spike-triggered power (STP) analysis revealed that the ability of

132   OB units to trigger beta power is stronger during ramp stimulation compared to baseline

133   periods (Pre: med: 6.694 µV², iqr: 2.291 – 16.447 µV²; Stim: med: 18.285 µV², iqr: 4.437 –

134   58.407 µV²; n_{units} = 309 from 19 mice, p = 3.16*10^{-13}, LMEM) (Figure 2I).

135   These data indicate that the activation of M/TCs recruits the local circuitry in the OB

136   and thereby organizes the OB network activity in the beta rhythm.
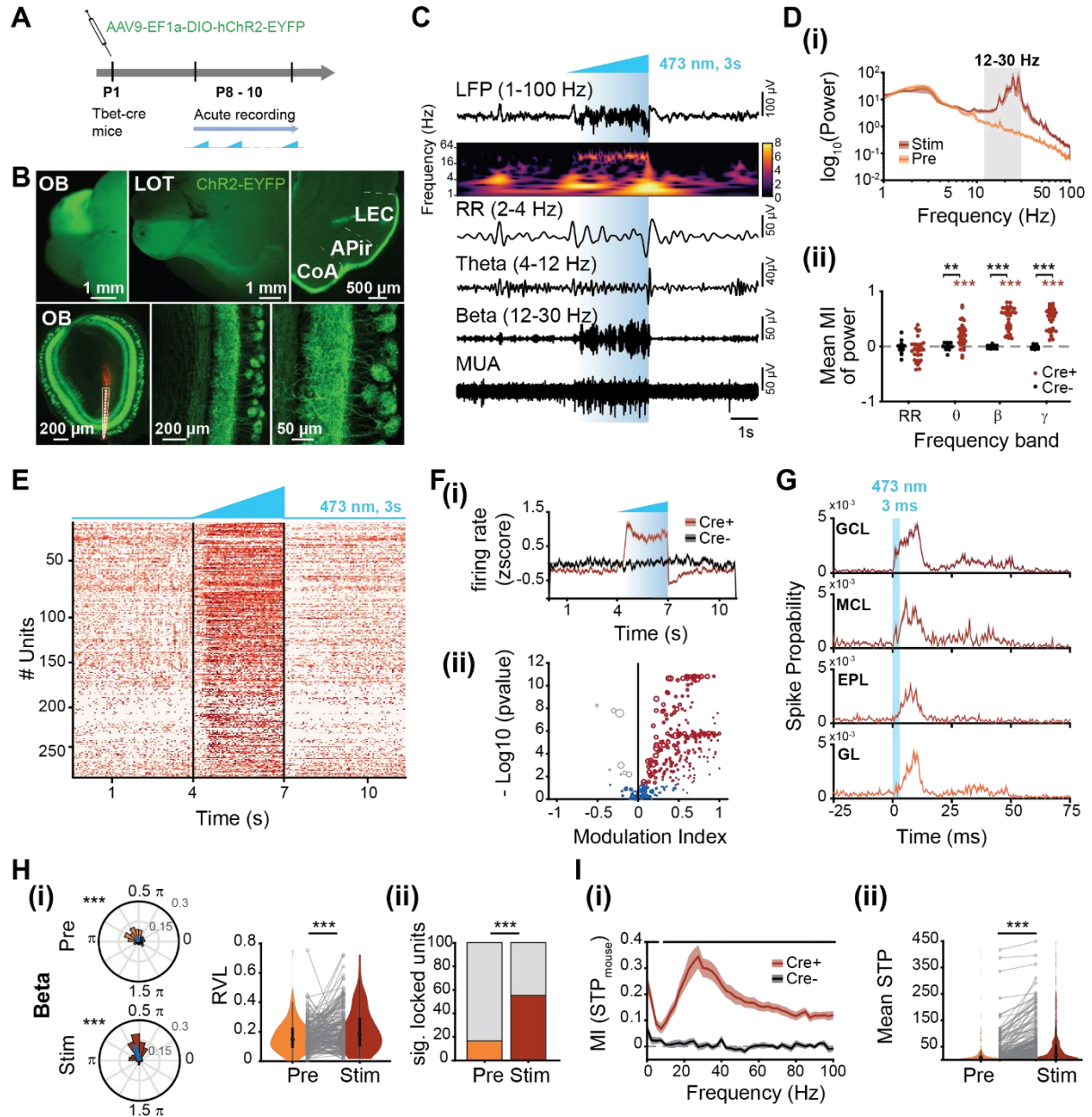
Figure 2: Effects of M/TC manipulation by light on single-unit entrainment and oscillatory activity in OB.

Figure 2: Effects of M/TC manipulation by light on single-unit entrainment and oscillatory activity in OB.

A. Schematic of the experimental protocol.

B. Top, photograph of the dorsal (left) and ventral side (middle) of a brain from a Tbet-cre+ mouse showing EYFP expression in the OB and M/TC axonal projections (LOT) to LEC, piriform transition area (APir), and cortical amygdala (CoA) (right). Bottom, digital photomontages displaying the DiI labeled electrode track in OB (left) and confocal images displaying the mitral cell layer (MCL) of the right OB at different magnifications (middle and right).

C. Representative extracellularly recorded LFP in the OB displayed band-pass filtered in different frequency bands and accompanied by the corresponding wavelet spectrum during ramp stimulation, as well as by the simultaneously recorded MUA in the MCL.

D. (i) Power spectrum for OB LFP before (orange) and during (red) ramp stimulation. The gray shaded area corresponds to the beta band (12-30 Hz). (ii) Mean MI of LFP power in different frequency bands for cre+ (red) and cre- (black) mice. (red stars for cre+: *** $p < 0.001$, Wilcoxon signed-rank test; black stars for comparison cre+ vs. cre-: ** $p < 0.01$, *** $p < 0.001$, Wilcoxon rank-sum test)

E. Raster plot of SUA in the OB before, during, and after ramp stimulation.

F. (i) Z-scored firing rate in response to ramp stimulation of units recorded in the OB of cre+ (red) and cre- (black) mice. (ii) MI of SUA firing in response to ramp stimulation (Significantly activated units are shown in red, whereas significantly inhibited units in gray, $p < 0.01$, Wilcoxon signed-rank test).

G. Spiking probability of units located in the granule cell layer (GCL), MCL, external plexiform layer (EPL), and glomerular layer (GL) after a 3 ms light pulse (blue box, 473 nm) delivered to the OB.

H. (i) Phase locking of OB units to beta oscillations in OB. Left, polar plots displaying phase locking of OB units before (Pre, orange) and during ramp stimulation (Stim, red). The mean resulting vectors are shown as blue lines. (*** $p < 0.001$, Rayleigh test for non-uniformity). Right, violin plots displaying the resulting vector length (RVL) of OB units before (Pre, orange) and during ramp stimulation (Stim, red). Gray dots and lines correspond to individual units. (*** $p < 0.001$, linear mixed-effect model). (ii) Percentage of significantly locked units before (Pre, yellow) and during (Stim, red) stimulation. (*** $p < 0.001$, Fisher's exact test).

I. (i) Plot of mean MI of spike-triggered power (STP) for cre+ (red) and cre- (black) mice during ramp stimulation. (black line: $p < 0.05$, Wilcoxon rank-sum test). (ii). Violin plots displaying mean STP for OB units before (Pre, yellow) and during ramp stimulation (Stim, red). Gray dots and lines correspond to individual units. (*** $p < 0.001$, linear mixed-effect model).

M/TC activation drives neuronal firing in LEC and HP

137 To characterize the downstream effects of beta band entrainment of OB, we firstly analyzed

138 the organization of OB projections in neonatal mice. In line with morphological investigations

139 in adult mice (Igarashi et al., 2021), we previously showed that MC axons are present in

140 superficial layers of LEC already at neonatal age (Gretenkord et al., 2019). Entorhinal neurons

141 in layer II/III strongly project to HP and weakly to PFC (Hartung et al., 2016a; Xu et al., 2021).

142 Here, we performed axonal tracing of M/TCs using the anterograde virus (AAV9-hSyn-

143 hChR2(H134R)-EYFP) injected into the OB at P8. Simultaneously, we monitored the entorhinal

144 neurons that project to HP by using the retrograde virus (AAVrg-CamKIIa-mCherry) injected

145 into the HP at P8 (Figure 3A, B). At P18, MC axons expressing EYFP were present in layer I/II

146 of LEC and PiR (Figure 3B). Additionally, mCherry-expressing HP-projecting neurons were

147 identified in entorhinal layer II/III. These neurons send their apical dendrites to layer I of LEC,

148 where they collocate with MC axonal projections (Figure 3B).

150   Since these morphological data suggest that the OB interacts with downstream cortical
151   areas, in a second step, we monitored the functional impact of direct OB projections on limbic
152   circuits. For this, we used pulse (3 ms) and ramp (3 s) blue light stimulations (473 nm) of
153   transfected OB neurons and simultaneously recorded the neuronal activity in LEC, HP, and
154   PFC. Pulse stimulation of M/TCs induced neuronal firing in all investigated brain areas, except
155   PFC (Figure 3Ci). While the light-evoked OB firing rate sharply peaked already 7-8 ms post-
156   stimulus, the responses in the other brain areas were substantially broader and delayed (37
157   ms in LEC, 45-60 ms in HP). A second firing increase was detected in OB after ~28 ms and
158   might reflect OB-internal processing or feedback activation from downstream areas. To expand
159   on these results, we used normalized cross-covariance analysis to uncover the temporal
160   correlations between light-evoked spike trains in the investigated brain regions. The most
161   prominent interaction was detected for OB-LEC, with OB firing preceding the entorhinal
162   discharges (Figure 3Cii). While having a similar directionality, the OB-HP cross-covariance
163   peaked later and less precisely. The data gives first insights into the communication pathways
164   relaying the information from M/TCs to LEC and subsequently, to HP.

165   Ramp stimulation of M/TCs evoked neuronal firing in LEC, HP, and PFC with similar
166   dynamics: a fast increase in OB followed by a delayed spiking in LEC, and subsequently in HP
167   and PFC. In OB, SUA abruptly increased with ramp onset (76.157 % of units activated
168   significantly, 2.847 % units inhibited significantly) and decreased post-stimulus (8.185 % of
169   units activated significantly, 29.893 % of units inhibited significantly) (Figure 3Di, Ei). In
170   contrast, the average SUA firing rate in LEC, HP, and PFC showed a delayed increase starting
171   around halfway through the ramp and continuing after the light stimulation (Figure 3Dii-iv).
172   Analysis of the proportion of activated units during and after ramp revealed that neurons in
173   downstream areas expressed higher firing rates also after the light was switched off (Figure
174   3E), indicating that the activation of M/TCs boosted the cortical network activation.
175   Correspondingly, this post-stimulus firing increase recruited more neurons than those activated
176   during ramp stimulation (LEC: 10.959 % during stimulation vs. 21.233 % post-stimulus; HP:
177   9.167 % vs. 10.833 %, PFC: 9.195 % vs. 19.540 %). In HP, the post-stimulus network effect
178   was not restricted to activation of neurons but also related to the increase in the proportion of
179   neurons that were inhibited after the ramp (7.5 % vs. 11.667 %). Light stimulation of control
180   animals did not change the average firing rate of units in all four investigated brain regions
181   (Figure S2A, B).

182   Thus, M/TC firing drives the activation of entorhinal, and subsequently, hippocampal
183   and prefrontal circuits.
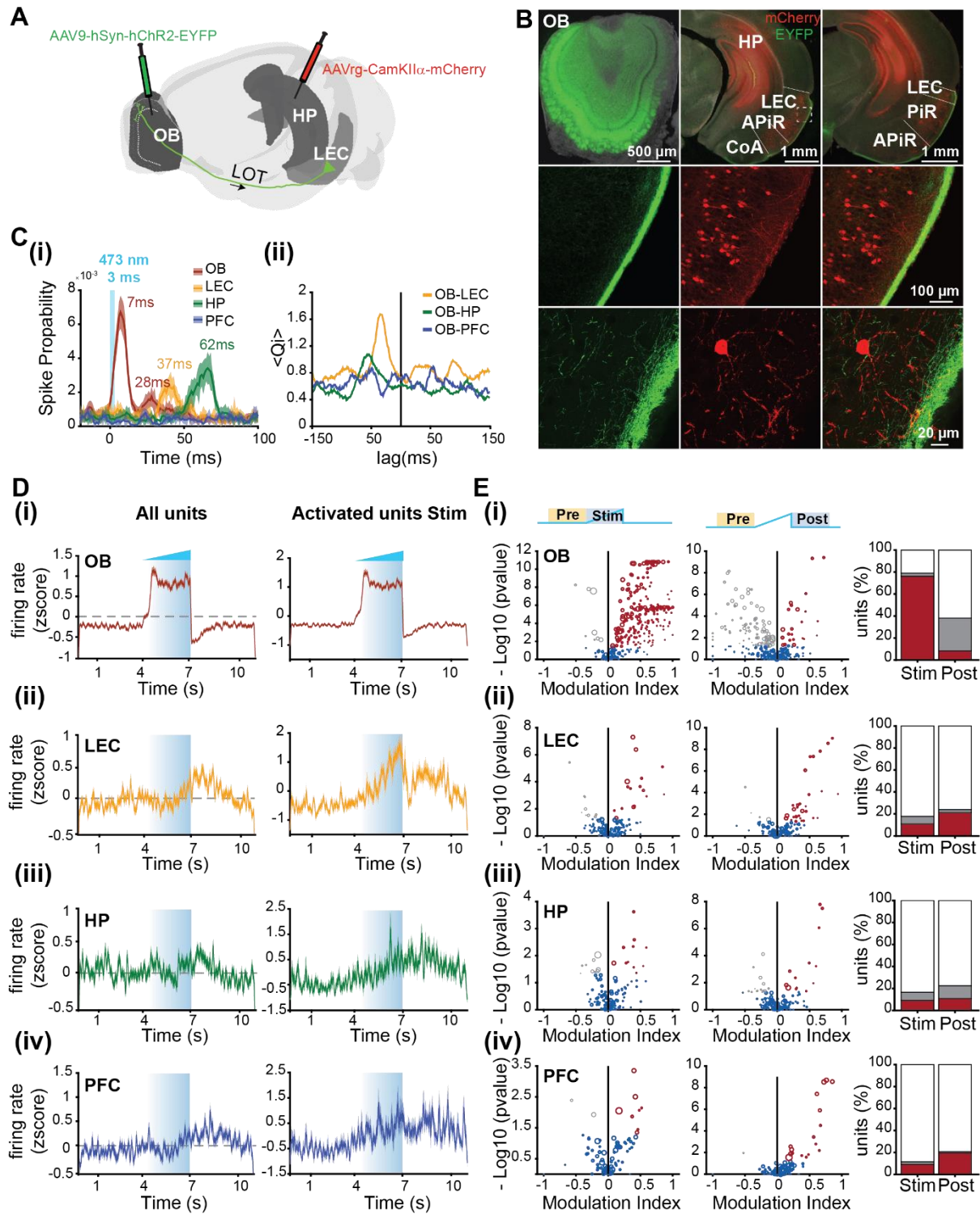
Figure 3: Effects of optogenetic manipulation of M/TCs on single-unit activity in LEC, HP, and PFC.

Figure 3: Effects of optogenetic manipulation of M/TCs on single-unit activity in LEC, HP, and PFC.

A. Schematic of the experimental protocol used to trace MC axons and neurons projecting to HP. (Brainrender: Claudi et al., 2020).

B. Top, digital photomontages displaying EYFP (green) and mCherry (red) fluorescence in coronal slices including OB (left, injection side of AAV9-hSyn-hChR2-EYFP), HP (middle, injection site of AAVrg-CamKIIα-mCherry), and LEC (right). Note the co-expression of EYFP and mCherry in LEC. Middle, EYFP (left), mCherry (middle), and their co-expression in the LEC are shown at larger magnification (dashed box). Bottom, EYFP (left), mCherry (middle), and their co-expression shown at larger magnification for a HP-projecting entorhinal neuron with dendrites targeting layer I.

C. (i) Spike probability of units in OB (red), LEC (yellow), HP (green), and PFC (blue) after a 3 ms light pulse (473 nm) delivered to the OB. Numbers indicate the delay of the peak spike probability for each brain area. (ii). Spike-spike cross-covariance for OB - LEC (yellow), OB - HP (green), and OB - PFC (blue). Negative lags correspond to OB activity driving spiking in other brain areas.

D. (i) Left, z-scored firing rate of units recorded in the OB of cre[+] (red) mice in response to light stimulation. Right, z-scored firing rate of significantly activated units during ramp stimulation. (ii) Same as (i) for units recorded in LEC (yellow). (iii) Same as (i) for units recorded in HP (green). (iv) Same as (i) for units recorded in PFC (blue).

E. (i) Left, volcano plot displaying the MI of SUA firing rates recorded in the OB before (Pre) vs. during (Stim) ramp stimulation (significant activated units are shown in red and significant inhibited units in gray, p < 0.01, Wilcoxon signed-rank test). Middle, same as the left image but for SUA firing rates before (Pre) vs. after (Post) ramp stimulation. Right, bar plots depicting the percentage of activated (red) and inhibited (gray) units during (Stim) and after (Post) ramp stimulation. (ii) Same as (i) for units recorded in LEC. (iii) Same as (i) for units recorded in HP. (iv) Same as (i) for units recorded in PFC.

M/TC activation boosts beta band coupling within downstream limbic circuits

184

185 The long-lasting effects of M/TC stimulation on the neuronal firing of downstream areas, LEC,

186 HP, and PFC suggest that OB activation might act as a driving force for the generation of

187 network oscillations in neonatal limbic circuits. To test this hypothesis, we paired ramp light

188 stimulation of ChR2-transfected M/TCs with LFP recordings in LEC, HP, and PFC of P8-10

189 mice. Ramp stimulation of M/TCs increased the oscillatory power in LEC, HP, and PFC (Figure

190 4A, B, Table S5). The most prominent increase was detected for beta band oscillations.

191 Moreover, we assessed the degree of synchrony between OB and cortical areas during light

192 stimulation by calculating the imaginary part of coherence, a measure that is insensitive to

193 false connectivity arising from volume conduction (Nolte et al., 2004). The imaginary coherence

194 between OB and LEC, OB and HP as well as OB and PFC increased during light activation of

195 M/TCs, the most prominent effects being detected in beta band range (Figure 4C, Table S6).

196 These results indicate that activation of M/TCs not only induces beta oscillations in OB

197 but also increases the 12-30 Hz oscillatory coupling between OB and downstream cortical

198 areas.
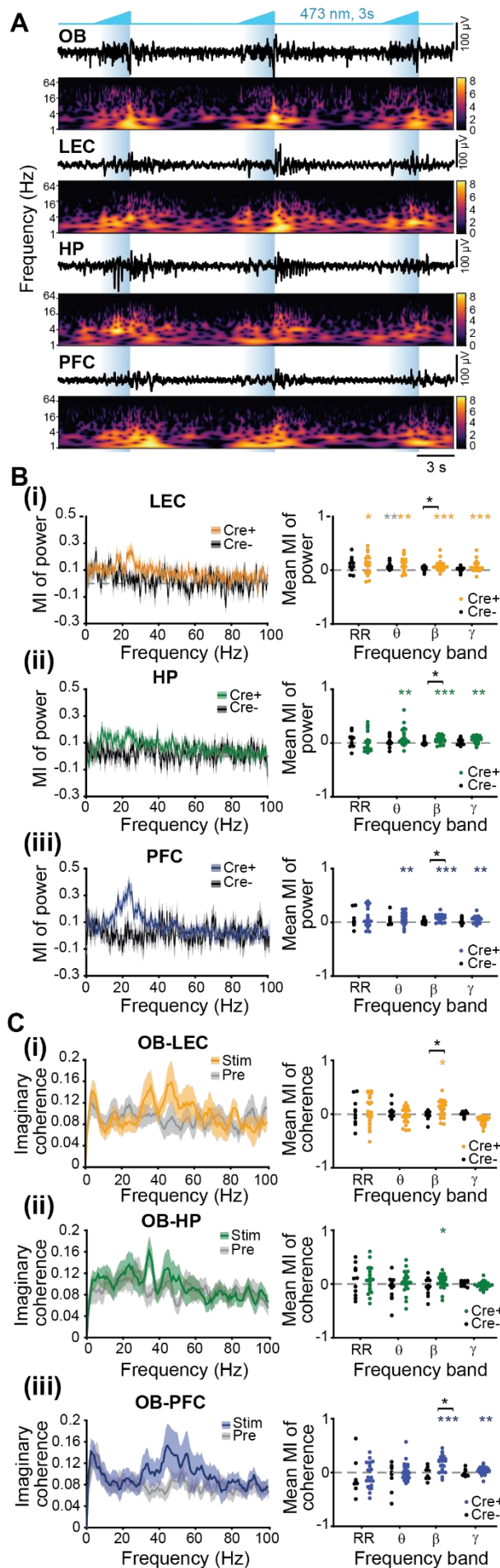
Figure 4: Oscillatory entrainment of limbic circuits as a result of M/TC activation by light.

A. Representative LFP traces recorded in the OB, LEC, HP, and PFC during ramp stimulation of ChR2-transfected M/TCs accompanied by the corresponding wavelet spectra.

B. (i) Left, plot of MI for power during ramp stimulation of oscillations in LEC for cre$^+$ (yellow) and cre$^-$ (black) mice. Right, MI of LFP power averaged for different frequency bands for cre$^+$ (yellow) and cre$^-$ (black) mice. (ii) Same as (i) for HP. (iii) Same as (i) for PFC. (colored stars for cre$^+$, gray stars for cre$^-$, * p < 0.05, ** p< 0.01, *** p < 0.001, Wilcoxon signed-rank test; black stars for comparison cre$^+$ vs. cre$^-$: * p < 0.05, Wilcoxon rank-sum test)

C. (i) Left, imaginary coherence between OB and LEC before (gray) and during (yellow) light stimulation. Right, MI of LFP coherence averaged for different frequency bands for cre$^+$ (yellow) and cre$^-$ (black) mice. (ii) Same as (i) for OB and HP. (iii) Same as (i) for OB and PFC. (colored stars for cre$^+$: * p < 0.05, ** p < 0.01, *** p < 0.001, Wilcoxon signed-rank test; black stars for comparison cre$^+$ vs. cre$^-$: * p < 0.05, Wilcoxon rank-sum test).

14

199 **Inhibition of M/TC output reduces oscillatory power as well as neuronal firing in OB,**
200 **LEC, and HP**

201 To elucidate whether M/TC activity is necessary for the generation of oscillatory activity in
202 downstream areas, we used inhibitory DREADDs (hM4D(Gi)) that block vesicle release when
203 expressed in M/TCs by cre-dependent virus vector injection (AAV9-EF1a-DIO-hM4D(Gi)-
204 mCherry) at P1 (Figure 5A). At P8, M/TC soma as well as their axons forming the lateral
205 olfactory tract (LOT), which targets the posterior part of the cerebrum, expressed hM4D(Gi)-
206 mCherry (Figure 5B). We performed extracellular recordings of LFP and SUA from OB, LEC,
207 and HP of P8-10 mice (n=35) before (baseline, 20 min) and after (40 min) subcutaneous
208 injection of C21 (3 mg/kg), a synthetic activator of DREADDs (Thompson et al., 2018) (Figure
209 5A). Since the impact of OB activation on PFC was rather weak, we did not monitor its activity
210 during OB silencing.

211 C21 caused broadband power reduction in OB that reached a maximum magnitude
212 within 5 min after the injection (Figure 5C, D, Table S7) and persisted for at least 2 h (Figure
213 S3C). The occurrence of discontinuous oscillatory events was lower after C21 injection in OB
214 (Figure 5F, Table S8), indicating that M/TC activity is involved in the generation of
215 discontinuous events in OB. Solely, the continuous RR in OB was not affected by the activation
216 of DREADDs (Figure 5E, Table S7). Moreover, silencing the M/TC output led to a broadband
217 reduction of oscillatory power in LEC and HP (Figure 5C-E, Table S7). Correspondingly, the
218 time spend in oscillatory events in LEC and HP decreased after inhibition of M/TC output
219 (Figure 5F, Table S8). In contrast, for cre$^-$ mice LFP power and time spend in oscillatory events
220 did not differ before and after C21 injection (Figure S4A, B, Table S7, 8).

221 Next, we monitored the effects of chemogenetic silencing of M/TCs on the neuronal
222 firing of downstream areas. Inhibitory DREADDs have been described to mainly reduce the
223 vesicle release in the expressing neurons, while having little, if any, impact on their ability to
224 generate action potentials (Roth, 2016; Stachniak et al., 2014). Indeed, C21 injection had a
225 weak effect on SUA in OB (cre$^+$: med MI: -0.071, iqr: -0.322 – 0.208, n=512, p=0.003, Wilcoxon
226 signed-rank test; cre$^-$: med MI: -0.028, iqr: -0.259 – 0.207, n=418, p=0.171, Wilcoxon signed-
227 rank test; cre$^+$ vs. cre$^-$: p=0.198, Wilcoxon rank-sum test) (Figure 5G, H). In particular, the
228 neuronal firing within the first 10 min after C21 injection decreased (Figure 5G), being most
229 likely the result of weaker network interactions within the OB. The DREADDs manipulation
230 affected not only the network and neuronal activity in OB but also the spike timing by
231 oscillations. In line with the results of spike-triggered power (STP) analysis, C21 injection
232 decreased the ability of SUA to entrain the OB in theta, beta, and gamma rhythms (Figure S4A,
233 Table S9). STP for RR was comparable in the presence and absence of C21 (Table S9). The
234 temporal relationship between OB spikes and oscillatory events in OB was also assessed by
235 calculating the phase-locking of SUA to RR and beta rhythm, respectively. In line with the

236   results of STP analysis, the phase-locking to beta (Baseline: med: 0.105, iqr: 0.061 – 0.152;

237   C21: med: 0.093, iqr: 0.053 – 0.139; n_{units}=524 from 16 mice, p=0.003, LMEM) was reduced

238   after C21 injection. In contrast, the phase coupling to RR (Baseline: med: 0.094, iqr: 0.051 –

239   0.153; C21: med: 0.159, iqr: 0.078 – 0.310; n_{units}=524 from 16 mice, p=$2.20*10^{-16}$, LMEM) was

240   increased after C21 injection (Figure S4B).

241   Silencing the M/TC output strongly reduced the LEC firing (cre^{+}: med MI: -0.420, iqr: -

242   0.598 – -0.108, n=126, p=$2.96*10^{-16}$, Wilcoxon signed-rank test; cre^{-}: med MI: 0.069, iqr: -

243   0.144 – 0.364, n=49, p=0.168, Wilcoxon signed-rank test; cre^{+} vs. cre^{-}: p=$3.87*10^{-10}$, Wilcoxon

244   rank-sum test), the effects lasting > 1 hour after C21 injection (Figure 5G, H). In contrast,

245   silencing of M/TC output had a shorter (~20 min) and weaker impact on hippocampal firing

246   (cre^{+}: med MI: -0.102, iqr: -0.438 – 0.230, n=102, p=0.036, Wilcoxon signed-rank test; cre^{-}:

247   med MI: -0.047, iqr: -0.256 – 0.109, n=74, p=0.119, Wilcoxon signed-rank test; cre^{+} vs. cre^{-}:

248   p=0.484, Wilcoxon rank-sum test).

249   These results indicate that silencing the M/TC output decouples neuronal firing from

250   beta oscillations in OB and decreases the oscillatory power and neuronal firing in LEC, as a

251   first downstream station of OB projections. On its turn, the weaker drive from LEC leads to

252   poor oscillatory entrainment of HP, yet without significant change of its neuronal firing.
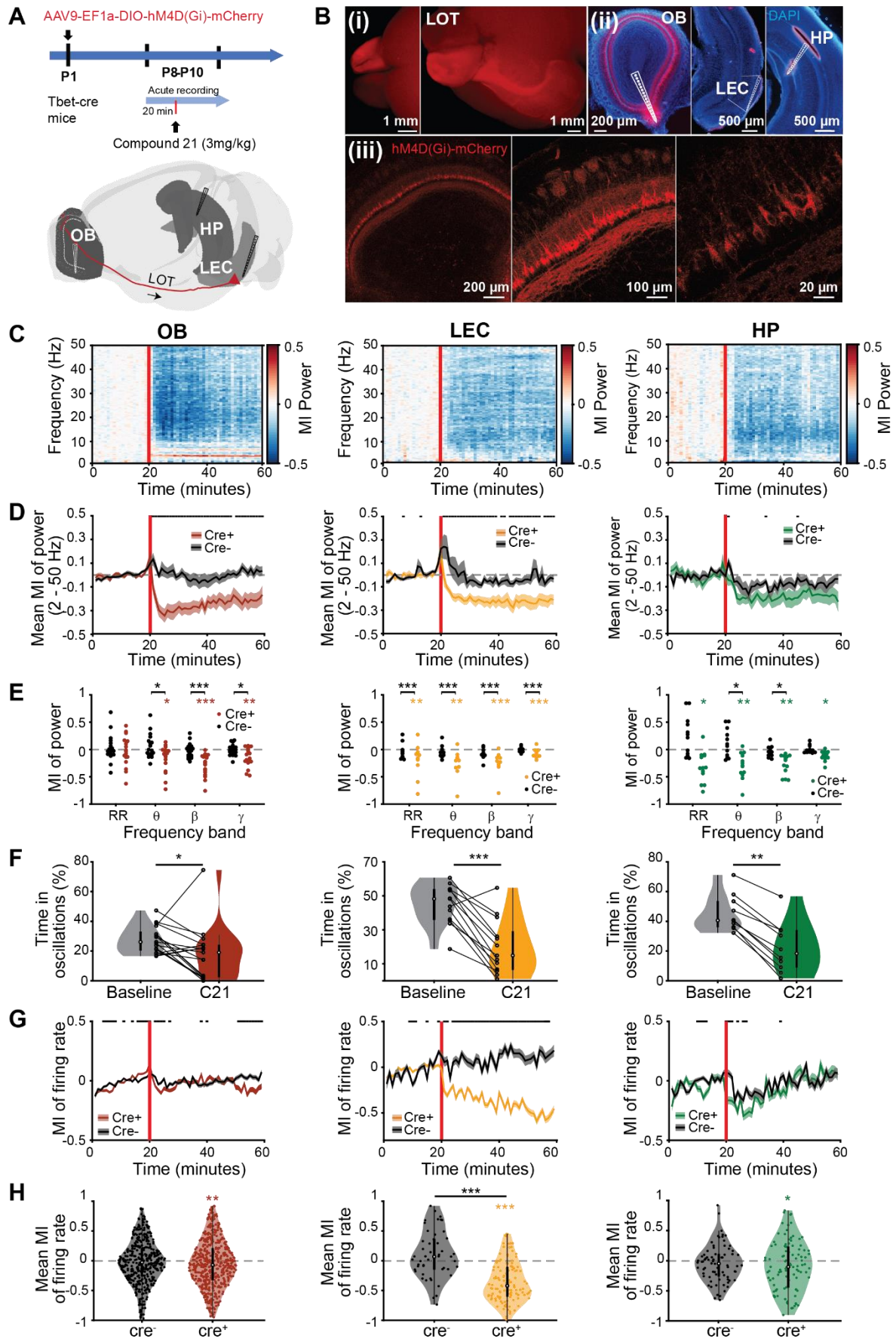
Figure 5: Effects of silencing M/TC output by inhibitory DREADDs on the oscillatory activity in OB, LEC, and HP.

Figure 5: Effects of silencing M/TC output by inhibitory DREADDs on the oscillatory activity in OB, LEC, and HP.

A. Top, schematic of the experimental protocol. Bottom, schematic of recording configuration for simultaneous extracellular recordings in OB, LEC, and HP (Brainrender: Claudi et al., 2020).

B. (i) Photograph of the dorsal (left) and ventral side (right) of a brain from a P8 Tbet-cre⁺ mouse showing mCherry (red) expression in the OB and M/TC axonal projections (LOT) to PIR and LEC. (ii) Digital photomontages displaying the DiI labeled electrode track (red) in DAPI (blue) stained slices including the OB (left), LEC (middle), and HP (right) from a P10 mouse. (iii) Confocal images displaying the MCL of the right OB at different magnifications. MC bodies, as well as dendrites, express mCherry.

C. Color-coded MI of LFP power before and after C21 injection in OB (left), LEC (middle), and HP (right). Vertical red lines correspond to the C21 injection.

D. Plots displaying the MI of LFP power averaged for 2 to 50 Hz before and after C21 injection in cre⁺ (colored) and cre⁻ (black) mice for OB (right, red), LEC (middle, yellow), and HP (right, green). Vertical red lines correspond to the C21 injection. (black line: $p < 0.05$, Wilcoxon rank-sum test).

E. MI of LFP power averaged for different frequency bands for cre⁺ (colored) and cre⁻ (black) mice for OB (left), LEC (middle), and HP (right). (Wilcoxon signed-rank test, colored stars for cre⁺: * $p < 0.05$, ** $p < 0.01$, *** $p < 0.001$; black stars for comparison cre⁺ vs. cre⁻: * $p < 0.05$, ** $p < 0.01$, *** $p < 0.001$, Wilcoxon rank-sum test)

F. Violin plots displaying the percentage of time spend in discontinuous oscillatory events before (Baseline, gray) and after C21 injection (C21, colored). Black dots and lines correspond to individual animals. (* $p < 0.05$, ** $p < 0.01$, *** $p < 0.001$, Wilcoxon signed-rank test)

G. Line plots displaying the MI of averaged SUA firing rates before and after C21 injection in cre⁺ (colored) and cre⁻ (black) mice for OB (left, red), LEC (middle, yellow), and HP (right, green). Vertical red lines correspond to the C21 injection. (black line: $p < 0.05$, Wilcoxon signed-rank test).

H. Violin plots displaying the MI of averaged SUA firing rates after C21 injection for cre⁻ (black) and cre⁺ mice (colored) recorded in OB (left, red), LEC (middle, yellow), and HP (right, green). Red and black dots correspond to individual units. (colored stars for cre⁺: * $p < 0.05$, ** $p < 0.01$, *** $p < 0.001$, Wilcoxon signed-rank test; black stars for comparison cre⁺ vs. cre⁻: *** $p < 0.001$, Wilcoxon rank-sum test)

Inhibition of M/TC output reduces the communication between OB and downstream cortical areas

To back up the hypothesis that the M/TC activity controls the developmental entrainment of limbic circuits, we monitored the communication between OB and downstream areas during silencing of M/TC output with DREADDs by using three distinct measures. First, we assessed the synchrony between OB, LEC, and HP by calculating the imaginary coherence in different frequency bands before (baseline) and after C21 injection (C21) (Figure 6A, B). MIs for beta coherence between OB and LEC, and OB and HP were significantly reduced after C21 injection. In contrast, the coherence in other frequency bands was not affected by C21 injection (Figure 6A, B, Table S10). Moreover, the C21-induced changes in the beta band were not detected in cre⁻ mice (Figure S6A, Table S10).

Second, we calculated the phase-amplitude coupling (PAC) to elucidate the role of M/TCs in the modulation of cortical beta oscillations by the RR phase in OB. C21 injection significantly reduced the z-scored PAC values between the OB RR phase and the amplitude of beta oscillations in LEC (Baseline: med: 2.499, iqr: 1.624 – 2.883; C21: med: 1.608, iqr:

268   0.674 – 2.361, n=13, p=0.017, Wilcoxon signed-rank test) and HP (Baseline: med: 2.363, iqr:

269   2.135 – 2.764; C21: med: 1.907, iqr: 1.319 – 2.248, n=10, p=0.037, Wilcoxon signed-rank test)

270   (Figure 6C). Additionally, fewer mice showed significant RR-beta PAC values after C21

271   injection (z-score > 1.96) in LEC (Baseline: 53.85% vs. C21: 39.77%) and HP (90% vs. 50 %).

272   Third, we tested the effect of C21 on the directionality of interactions between OB, LEC,

273   and HP (Figure 6D). We calculate the SDR and found that the prominent drive from OB to LEC

274   was absent after silencing of M/TC output, the values for OB → LEC and LEC → OB being

275   comparable (Figure 6Di, Table S11,12). Similarly, the drive from OB to HP was disrupted by

276   C21 injection (Figure 6Diii, Table S11,12). In contrast, the directionality of interactions between

277   LEC and HP was not affected by C21 injection. As reported for the baseline conditions, the

278   mutual interactions LEC-HP persisted after M/TC silencing (Figure 6Dii, Table S11,12).

279   Moreover, the C21-induced changes in directionality were not detected in cre⁻ mice (Figure

280   S5B, Table S11,12).

281   Thus, these results show that the M/TC activity is critical for the communication

282   between OB and its downstream cortical areas.
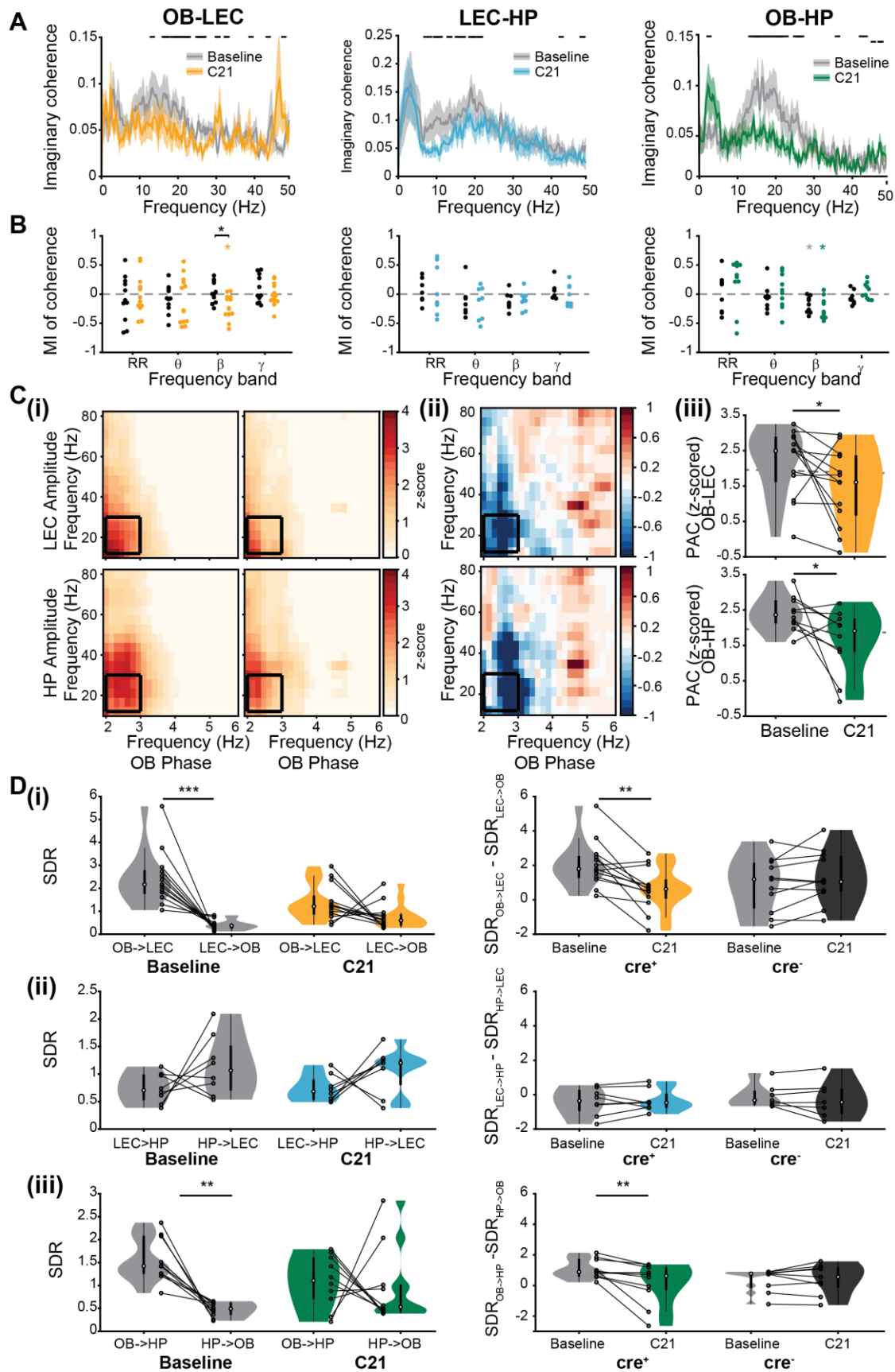
Figure 6: Modulation of functional communication within olfactory-cortical networks through silencing the M/TC output by inhibitory DREADDs.

Figure 6: Modulation of functional communication within olfactory-cortical networks through silencing the M/TC output by inhibitory DREADDs.

A. Imaginary coherence calculated for OB - LEC (left, yellow), LEC - HP (middle, light blue), and OB - HP (right, green), before (Baseline, gray) and after C21 injection (C21, colored). (black line: $p < 0.05$, Wilcoxon rank-sum test).

B. MI of coherence averaged for different frequency bands between OB and LEC (left, yellow), LEC and HP (middle, light blue), and OB and HP (right, green), for cre+ (colored) and cre- (black) mice. (colored stars for cre+, gray stars for cre-: * $p < 0.05$, Wilcoxon signed-rank test; black stars for comparison cre+ vs. cre-: * $p < 0.05$, Wilcoxon rank-sum test)

C. (i) Z-scored phase-amplitude coupling (PAC) between OB phase and LEC (top) and HP (bottom) amplitude, before (Baseline) and after C21 injection (C21). (ii) Difference of PAC values after and before C21 injection for OB - LEC (top) and OB - HP (bottom). (iii) PAC averaged for RR-beta coupling (black box in (i)) for OB - LEC (top) and OB - HP (bottom), before (Baseline, gray) and after C21 injection (colored). Dotted gray line corresponds to a z-score of 1.96. (* $p < 0.05$, Wilcoxon signed-rank test).

D. (i) SDR calculated for OB and LEC. Left, SDR values for OB -> LEC and LEC -> OB before (Baseline, gray) and after C21 injection (C21, yellow). Right, difference of SDR values for both directions for cre+ and cre- mice. (ii) Same as (i) for LEC and HP (blue). (iii) Same as (i) for OB and HP (green). Black dots and lines correspond to individual animals. (** $p < 0.01$, *** $p < 0.001$, Wilcoxon signed-rank test).

DISCUSSION

Long-range interactions within limbic circuits emerge early in life (Chini and Hanganu-Opatz, 2021), yet it is still unknown whether the coordinated activity patterns underlying the coupling are endogenously generated or result through the driving force of sensory systems. Besides muscle twitches (Rio-Bermudez and Blumberg, 2018) and passive tactile sensation, olfactory inputs are likely candidates for the instruction of limbic circuitry development. Newborn rodents are not only able to smell from birth on but, importantly, also use olfactory information for learning and cue-directed behaviors such as localization of the nipples of the dam (Logan et al., 2012; Welker, 1964). A first piece of evidence for the critical role of olfaction for limbic development is the fact that the neonatal OB shows functional coupling with the LEC, the gatekeeper of the limbic circuitry, during discontinuous network oscillations in the theta-beta frequency range as well as in the continuous respiration-related rhythm (RR) (Gretenkord et al., 2019). Here, we extended these findings and uncovered that MC firing sets a beta band entrainment also in downstream areas, such as HP and PFC. The temporal dynamics of oscillatory and firing activity revealed that even in periods without active odor sampling, OB drives the activation of limbic circuits.

Layer-specific analysis of SUA revealed that M/TC activation leads to a complex entrainment of the OB microcircuit that results in augmented firing rate also for interneurons in the GCL, EPL, and GL. Experimental and modeling studies have shown that both beta and gamma oscillations in the OB rely on dendro-dendritic interactions between M/TCs and GCs (David et al., 2015; Fourcaud-Trocmé et al., 2014; Neville and Haberly, 2003; Osinski et al., 2018; Osinski and Kay, 2016). In adults, the emergence of gamma and beta oscillations is

305 controlled by different excitability states of GCs as well as their dependency on centrifugal
306 input, with beta oscillations relying on a higher GC excitability and centrifugal feedback
307 projections (David et al., 2015; Martin et al., 2006; Osinski and Kay, 2016). However, gamma
308 oscillations are absent in the neonatal OB, most likely as a result of the late functional
309 integration of interneurons into local circuits and the different biophysical properties of MCs
310 and GCs during development (Dietz et al., 2011; Fletcher et al., 2005; Yu et al., 2015). Instead,
311 discontinuous beta band oscillations are present not only in OB but also in other sensory and
312 limbic areas (Bitzenhofer et al., 2017b). In the neonatal PFC, they have been shown to
313 accelerate along development until reaching the gamma band range at juvenile age
314 (Bitzenhofer et al., 2020). Similarly, acceleration of beta to gamma oscillations takes place in
315 V1 during the critical period for vision (Chen et al., 2015; Hoy and Niell, 2015). Whether the
316 beta band activity in OB undergoes a similar transition to faster rhythms and how this process
317 is controlled by interactions within OB and by feedback projections from PiR and LEC remain
318 to be elucidated.

319   The present data show that the OB network activation entrains downstream cortical
320 areas in beta oscillations. In adult rodents, the axonal terminals of MCs have been found to
321 target fan and pyramidal neurons in LII/III of LEC that, on their turn, relay this information to
322 the HP (Schwerdtfeger et al., 1990; Wouterlood and Nederlof, 1983). The axonal projections
323 from layer II/III LEC pyramidal neurons to CA1 are involved in associative odor learning in
324 adults (Li et al., 2017). Already at neonatal age, MC axons reach layer I of LEC (Gretenkord et
325 al., 2019; Walz et al., 2006). Here, projections of layer II/III neurons that target the HP were
326 detected and they might establish synaptic contacts with the MC axons. Optogenetic
327 stimulation revealed that the activation of M/TCs induced delayed firing of LEC neurons and
328 HP neurons, indicating that the pathway OB-to-HP is indeed already functional from birth on.
329 CA1 receives entorhinal input not only via the direct performant path but also through the tri-
330 synaptic path, spanning DG and CA3 (Basu et al., 2016). The long latency (~ 60 ms) in light-
331 induced CA1 firing might, therefore, be partly mediated by the tri-synaptic path. Of note, it was
332 recently shown that a distinct but rather small population of LEC layer II neurons directly
333 projects to the neonatal PFC (Xu et al., 2021), yet light stimulation of M/TCs did not recruit it.

334   Coordinated activity patterns in OB organized by MCs promote not only neuronal firing
335 but also network activation in downstream areas. Ramp light stimulation of M/TCs led to an
336 increase of beta band power in LEC, HP, and PFC. This power surge was accompanied by
337 increased long-lasting SUA firing in all three brain areas, indicating that the initial activation of
338 neurons is followed by activation of the local networks in LEC, HP, and PFC. Conversely,
339 blocking vesicle release on MC synapses by DREADDs reduced the broadband power as well
340 as neuronal firing in LEC and HP. Moreover, coherence analysis revealed increased

341 oscillatory, mainly beta band coupling, between OB and cortical areas during ramp stimulation,
342 whereas inhibition of M/TCs vesicle release reduced the drive OB → LEC and OB → HP as
343 well as RR-beta cross-frequency coupling between OB-LEC and OB-HP. While the artificial
344 activation of MCs might not be entirely comparable to the neural processes underlying odor
345 sampling and processing during a learning task, these results identify the beta rhythm as a
346 potential mechanism of long-range communication between OB and downstream cortical
347 networks.

348   What might be the relevance of OB-controlled beta band activation of cortical circuits
349 during early postnatal development? Beta oscillations have been reported to play a key role in
350 working memory and decision making in adult humans (Spitzer and Haegens, 2017). Further,
351 prominent beta band synchrony between cortical areas has been identified during olfactory-
352 guided memory and decision making tasks in rodents (Igarashi et al., 2014; Martin et al., 2007;
353 Rangel et al., 2016; Symanski et al., 2021). A similar, but sniffing-independent increase in
354 hippocampal beta oscillations has been observed during an object learning task (Iwasaki et
355 al., 2021). Moreover, the firing of beta-entrained CA1 interneurons during an odor-place
356 associative memory and decision-making task related to an accurate performance, indicating
357 that beta oscillations enable temporal coordination and recruitment of neurons within functional
358 cell assemblies (Rangel et al., 2016; Symanski et al., 2021). In line with these experimental
359 data, modeling confirmed that beta oscillations optimally contribute to the coupling of cell
360 assemblies over long axonal conductance delays (Bibbig et al., 2002; Kopell et al., 2011,
361 2000). During development, discontinuous beta band events that have been identified in PFC,
362 HP, and LEC might facilitate the formation of initial cell assemblies with relevance for cognitive
363 performance later in life. We previously showed that interfering with beta band oscillations
364 during a defined developmental period causes network miswiring and poor behavioral
365 performance of adult mice (Bitzenhofer et al., 2021). Similarly, in a mouse model of psychiatric
366 risk reduced beta band activity at neonatal age has been found to correlate with later cognitive
367 deficits (Chini et al., 2020; Xu et al., 2021). Here, we identified the olfactory activity as a
368 prominent driver of these early beta oscillations. The results let us hypothesize that transient
369 disturbance of neonatal olfactory processing precludes the functional refinement of entorhinal-
370 hippocampal-prefrontal circuits, ultimately leading to cognitive deficits in adulthood. Further
371 research is warranted to directly test this hypothesis and elucidate the role of early activity
372 patterns in OB for cognitive development.

373

374

375

376

MATERIALS AND METHODS

Ethical Approval

All experiments were performed in compliance with the German laws and the guidelines of the European Union for the use of animals in research (European Union Directive 2010/63/EU) and were approved by the local ethical committee (Behörde für Gesundheit und Verbraucherschutz Hamburg, ID 15/17).

Animals

Time-pregnant C57Bl/6/J and Tbet-cre mice from the animal facility of the University Medical Center Hamburg-Eppendorf were housed individually in breeding cages at a 12h light / 12h dark cycle and fed ad libitum. Offspring (both sexes) where injected with either AAV9-Ef1a-DIO-hChR2(E123T_T159C)-EYFP (Addgene, Plasmid #35509) or AAV9-EF1a-DIO-hM4D(Gi)-mCherry (Addgene, Plasmid #50461) virus at postnatal day (P) 0 or 1. Genotypes were determined using genomic DNA and following primer sequences (Metabion, Planegg/Steinkirchen, Germany) as described previously (Gretenkord et al. 2019): for Cre: PCR forward primer 5′-ATCCGAAAAGAAAACGTTGA-3′ and reverse primer 5′-ATCCAGGTTACGGATATAGT-3′. The PCR reactions were as follows: 10 min at 95 °C, 30 cycles of 45 s at 95 °C, 90 s at 54 °C, and 90 s at 72 °C, followed by a final extension step of 10 min at 72 °C. In addition to genotyping, EGFP expression in OB was detected using a dual fluorescent protein flashlight (Electron microscopy sciences, Hatfield, PA, USA) prior to surgery. At P8-10 cre⁻ and cre⁺ mice underwent light stimulation or Compound 21 injections and *in vivo* multi-side electrophysiological recordings.

Surgical procedures and recordings

Virus injection for transfection of MTCs with ChR2 and hm4D(Gi)

For transfection of M/TCs with the ChR2 derivate E123T/T159C or inhibitory DREADDs (hm4D(Gi)), P0-1 pups were fixed into a stereotaxic apparatus and received unilateral injections of one of two viral constructs (AAV9-Ef1a-DIO hChR2(E123T/T159C)-EYFP, 200 µl at titer ≥ 1×10¹³ vg/mL, Plasmid, #35509, Addgene, MA, USA; AAV9-EF1a-DIO-hM4D(Gi)-mCherry, 200 µl at titer ≥ 1×10¹⁴ vg/mL Plasmid #50461, Addgene, MA, USA). The virus was produced by Addgene or the Virus Facility of the University Medical Center Eppendorf. A total volume of 200 nl was slowly (200 nl/min) delivered at a depth of around 0.5 mm into the right OB using a micropump (Micro4, WPI, Sarasota, FL). Following injection, the syringe was left in place for at least 30 s to avoid reflux of fluid. Pups were maintained on a heating blanket until full recovery and returned to the dam.

Virus injection for tracing

For the transfection of M/TC axons with EYFP and the retrograde labeling of HP-projecting neurons with mCherry, P0-1 pups received the viral construct AAV9-hSyn-hChR2(H134R)-EYFP (200 µl at titer ≥ 1×10^{13} vg/mL, #26973-AAV9, Addgene, MA, USA) into the OB and the retrograde virus AAVrg-CamKIIα-mCherry (80 µl at titer ≥ 7×10^{12} vg/mL, #114469-AAVrg, Addgene, MA, USA) into the HP. Virus injection was performed similarly as for the transfection of M/TCs with ChR2 or hm4D(Gi). After 10 days, the brains of investigated mice were perfused with 4% paraformaldehyde (PFA), sliced and MC axons and HP-projecting neurons in LEC and PIR were imaged using a confocal microscope.

Surgical procedure for electrophysiology

For in vivo recordings, P8-10 mice underwent surgery according to previously described protocols (Brockmann et al., 2011; Gretenkord et al., 2019; Kostka et al., 2020). Under isoflurane anesthesia (induction: 5 %, maintenance: 2.5 %, Forane, Abbott), the skin above the skull was removed and 0.5 % bupivacaine / 1 % lidocaine was locally applied on the neck muscles. Two plastic bars were mounted on the nasal and occipital bones with dental cement. The bone above the right OB (0.5-0.8 mm anterior to frontonasal suture, 0.5 mm lateral to inter-nasal suture), LEC (0 mm posterior to lambda, 6-7.5 mm lateral from the midline), HP (2.5 mm anterior to lambda, 3.5 mm lateral from the midline) and PFC (0.5 mm anterior to bregma, 0.1-0.5 mm lateral from the midline) was carefully removed by drilling a hole of < 0.5 mm in diameter. Throughout surgery and recording session the mice were maintained on a heating blanket at 37°C.

Multi-site electrophysiological recordings in vivo

Three-side or four-side recordings were performed in non-anesthetized P8-10 mice. For this, one-shank electrodes (NeuroNexus, MI, USA) with 16 recording sites (0.4-0.8 MΩ impedance, 50 µm inter-site spacing for recordings in OB and HP, 100 µm inter-site spacing for recordings in LEC and PFC) were inserted into OB (0.5-1.8 mm, angle 0°), LEC (for 4-side recordings, depth: 2 mm, angle: 180°; for 3-side recordings, depth: 2-2.5 mm, angle: 10°), HP (1.3-1.9 mm, angle 20°) and PFC (1.8-2.1 mm, angle 0°). For light stimulation one-shank optrodes (NeuroNexus, MI, USA) with the same configuration as the electrodes were inserted in the OB. Before insertion, the electrodes were covered with DiI (1,1'-Dioctadecyl-3,3,3',3'-tetramethylindocarbocyanine perchlorate, Molecular Probes, Eugene, OR). A silver wire was inserted into the cerebellum and served as a ground and reference electrode. Before data acquisition, a recovery period of 20 min following the insertion of electrodes was provided. Extracellular signals were band-pass filtered (0.1 Hz-9 kHz) and digitized (32 kHz or 32,556 kHz) by a multichannel amplifier (Digital Lynx SX; Neuralynx, Bozeman, MO; USA) and Cheetah acquisition software (Neuralynx). Spontaneous activity was recorded for at least 20

448   min before light stimulation or Compound 21 (C21, Hellobio, Ireland) injection. The position of

449   recording electrodes in OB, LEC, HP, and PFC was confirmed after histological assessment

450   *post-mortem.* For the analysis of LFP in OB, the recording site centered in the EPL was used,

451   whereas for HP the recording site located in the CA1 was considered. For analysis of LFP in

452   LEC only recording sites that were histologically confirmed to be located in superficial

453   entorhinal layers were used. Similarly, only recordings sites confined to the prelimbic sub-

454   division of PFC were considered. For the analysis of spiking activity, all recording sites

455   confirmed to be located in the areas of interest (OB, LEC, HP, and PFC) were considered.

456   When necessary, spikes recorded in OB were assigned to specific layers according to the

457   location of recording sites.

Morphology

459   Mice were anesthetized with 10% ketamine (Ketamidor, Richter Pharma AG, Germany) / 2%

460   xylazine (Rompun, Bayer, Germany) in 0.9% NaCl solution (10 μg/g body weight, i.p.) and

461   transcardially perfused with Histofix (Carl Roth, Germany) containing 4% PFA. Brains were

462   postfixed in 4% PFA for 24 h and sliced. Slices (100 μm-thick) were mounted with Fluoromount

463   containing DAPI (Sigma-Aldrich, MI, USA). The positions of the DiI-labeled extracellular

464   electrodes in the OB, LEC, HP, and PFC were reconstructed to confirm their location. Virus

465   expression was verified by EYFP (for ChR2) or mCherry (for hM4D(Gi)) fluorescence in the

466   right OB. For confocal imaging of EYFP or mCherry fluorescence in M/TCs, HP, and LEC, 50

467   μm-thick slices mounted with Vectashield (CA, USA) were used.

Light stimulation

469   Activation of M/TCs was achieved by either ramp or pulse light stimulation applied using a

470   diode laser (473 nm; Omicron, Austria) which was controlled by an arduino uno (Arduino, Italy).

471   For ramp stimulation, a light stimulus with linear increasing power (3 s rise time) was presented

472   30-60 times. For pulse stimulation 3 ms light pulses at 2 Hz were delivered. Laser power was

473   adjusted for every recording (1.37-5.15 mW) to reliably induce neuronal firing.

Compound 21 injection

475   Compound 21 (3 mg/kg solved in 0.9% NaCl) was injected subcutaneously after >20 min

476   recording of baseline activity, while the mouse was fixed in the stereotaxic apparatus. The

477   activity was recorded for 40-120 min post-injection.

Data Analysis

479   *LFP analysis.* Data were analyzed offline using custom-written scripts in the MATLAB

480   environment (MathWorks, Natick, MA). Data were first low-passed filtered (<100 Hz) using a

481   third-order Butterworth filter before down-sampling by factor 20 to 1.6 kHz to analyze LFP. All

482   filtering procedures were performed in a manner preserving phase information.

483 *Detection of oscillatory activity.* Discontinuous network oscillations in the LFP recorded from
484 OB, LEC, and HP before and after C21 injection were detected using a previously developed
485 unsupervised algorithm (Cichon et al., 2014). Briefly, deflections of the root mean square of
486 band-pass filtered (4-100 Hz) signals exceeding a variance-depending threshold (2 times the
487 standard deviation from the mean) were assigned as oscillatory periods. Only oscillatory
488 periods lasting at least 1 s were considered for analysis.

489 *Power spectral density.* Power spectral density was analyzed for either the entire baseline
490 period, 2 s long periods before (Pre), and during light ramp stimulation (Stim) for recordings
491 combined with optogenetic manipulation. For recordings paired with DREADD manipulation,
492 the power was either calculated for every minute or averaged for the entire baseline period (19
493 min) and post C21 injection period (30 min). Power was calculated using Welch's method with
494 non-overlapping windows of 2 s (ramp periods) or 3 s length. Time-frequency plots of power
495 were calculated with a continuous wavelet transform (Morlet wavelet).

496 *Coherence.* The imaginary part of coherence, which is insensitive to volume-conduction-based
497 effects (Nolte et al., 2004), was calculated for the same time periods as the power by taking
498 the absolute value of the imaginary component of the normalized cross-spectrum:

499

500
$$C_{XY}(f) = \left| Im \left(\frac{P_{XY}(f)}{\sqrt{P_{XX}(f)P_{YY}(f)}} \right) \right|.$$

501 *Spectral Dependency Ratio.* The Spectral Dependency Ratio (SDR) was calculated according
502 to Shajarisales et al. (Shajarisales et al., 2015) from the power spectral densities ($S_x(f)$ and
503 $S_y(f)$) of the signals X and Y:

504
$$SDR_{X \to Y} = \frac{mean\left(S_y(f)\right)}{mean(S_x(f)) * mean\left(\frac{S_y(f)}{S_x(f)}\right)}$$

505
$$SDR_{Y \to X} = \frac{mean(S_x(f))}{mean\left(S_y(f)\right) * mean\left(\frac{S_x(f)}{S_y(f)}\right)}$$

506 The most likely direction of causation is the one having significantly larger SDR values.
507 (https://github.com/OpatzLab/HanganuOpatzToolbox/tree/master/LFP analysis/getSDR.m)

508 *Spiking analysis.* Single units were automatically detected and clustered using the python-
509 based software klusta (Rossant et al., 2016) and manually curated using phy
510 (https://github.com/cortex-lab/phy). The firing rate was computed by dividing the total number
511 of spikes by the duration of the analyzed time window. To assess the spike probability,
512 histograms of spike count using 1 ms bins were calculated for periods around the light pulse
513 (50 ms before to 150 ms after) and normalized to the number of delivered light pulses. Cross-

514   covariance of spike trains was calculated as described previously (Gretenkord et al., 2019;

515   Siapas et al., 2005). Briefly, cross-covariance for two spike trains N_i and N_j, was estimated

516   from the cross-correlation histogram ($J_{ij}^{T,b}(u)$) as follows:

517
$$\hat{q}_{ij}(u) = \frac{J_{ij}^{T,b}(u)}{bT} - \hat{P}_i\hat{P}_j,$$

518   (b = binsize, T observation period, $\hat{P}_i = \frac{N_i(T)}{T}$, $\hat{P}_j = \frac{N_j(T)}{T}$). The standardized cross-covariance

519   was calculated as

520
$$Q_{ij}(u) = \sqrt{\frac{bT}{P_iP_j}}\,\hat{q}_{ij}(u),$$

521   with P_i, P_j being the mean firing rates. Only pairs of units with firing rates > 0.05 Hz and

522   significant standardized cross variance were considered. The Null hypothesis was rejected

523   when $|Q_{ij}(u)| > Z_\alpha$. ($Z_\alpha = \sqrt{2}erf^{-1}\left(\frac{1-\alpha}{N_{lags}}\right)$; two-tailed critical z value at level α = 0.01). The

524   standardized mean cross-variance for one unit was calculated as

525
$$Q_i(u) = \sqrt{\frac{1}{K}\sum_{j=1}^{K} Q_{ij}(u)},$$

526   (*K*=number of units in 2. Region) and the mean for all unit pairs as: $\langle Q_i(u) \rangle = \frac{1}{L^2}\sum_{i=1}^{L} Q_i(u)$.

527   *Modulation index.* The modulation index (MI) of power, coherence, firing rate, and STP for light

528   stimulation or DREADD manipulation was calculated as

529
$$MI = \frac{Value_{Stim} - Value_{Pre}}{Value_{Stim} + Value_{Pre}}.$$

530   *Spike-LFP coupling.* Phase locking of spiking units to network oscillations was assessed using

531   a previously described algorithm (Siapas et al., 2005). For this, the LFP signal was bandpass

532   filtered (2-4 Hz (RR), 4-12 Hz (theta), 12-30 Hz (beta), 30-100 Hz (gamma)) using a third-order

533   Butterworth filter. The instantaneous phase was extracted using the Hilbert transform on the

534   filtered signal. The coupling between spikes and network oscillations was tested for

535   significance using the Rayleigh test for non-uniformity. For analysis of baseline properties

536   (Figure 1) only neurons that showed significant phase locking were considered for the analysis

537   of the mean phase angle and the locking strength, which was calculated as mean resulting

538   vector length (RVL). For paired comparison of RVLs (Figure 2, S1, S4) all units with a firing

539   rate higher than 0.01 Hz during baseline (18 min) and after C21 injection (18 min, DREADD

540   manipulation) or more than 10 spikes before (Pre) and during (Stim) light ramp pulses were

541   considered.   (https://github.com/OpatzLab/HanganuOpatzToolbox/blob/master/Spikes-LFP

542   analysis/getPPC_PLV.m)

543   *Spike-triggered power.* Spike-triggered power (STP) was calculated for the same time periods
544   as RVL by taking the mean of the LFP power for 0.4 s long time windows centered on each
545   spike.

546   *Phase-amplitude coupling.* Phase-amplitude coupling (PAC) between RR phase in OB and
547   beta band amplitude in LEC and HP was calculated as previously described (Tort et al., 2010).
548   Briefly, the LFP signals were bandpass filtered and the Hilbert transform was used to extract
549   the phase and amplitude, respectively. Subsequently, the amplitude of the beta-filtered signal
550   in LEC or HP was determined at each phase of the filtered OB signal. The phase was divided
551   into 16 bins and the mean amplitude for each bin was calculated and normalized to the total
552   number of bins. The normalized modulation index (MI) was calculated as the deviation between
553   an empirical and uniform amplitude distribution. MI matrices were z-scored and the average
554   was calculated for RR (2-3 Hz) – beta (12-30 Hz) coupling.

555   ### Statistics
556   Statistical analysis was performed in MATLAB environment or R Statistical Software. As none
557   of the data sets were normally distributed, data were tested for significance using Wilcoxon
558   rank-sum test (2 unrelated samples) or Wilcoxon sign-rank test (2 related samples). Data
559   (except phase values) are presented as median (med) and interquartile range (iqr). Outlier
560   removal was applied to paired data points if the distance of their difference from the 25th or 75th
561   percentile exceeds 2.5 times the interquartile interval of their difference. Phase locking was
562   tested for significance using the Rayleigh test for non-uniformity. Phase angles were compared
563   using a circular non-parametric multi-sample test for equal medians. Differences in proportions
564   were tested using Fisher's exact test. Nested data were analyzed with linear mixed-effects
565   models (LMEM) using animals as a fixed effect. Significance levels *$p<0.05$, **$p<0.01$ and
566   ***$p<0.001$ were considered. If not included in the text, values and corresponding test statistics
567   of all presented data can be found in the supplementary material (Table S1-12).

568

569

570

571

572

573

574

575

576

Additional Information

Author Contributions

I.L.H.-O. and J.K.K conceived the study and designed the experiments. J.K.K carried out the experiments and analyzed the data. J.K.K, and I.L.H.-O. interpreted the data. J.K.K. and I.L.H.-O. wrote the article. All authors discussed and commented on the manuscript.

Declaration of Interests

The authors declare no competing interests.

REFERENCES

Ackman JB, Burbridge TJ, Crair MC. 2012. Retinal waves coordinate patterned activity throughout the developing visual system. *Nature* **490**:219–225. doi:10.1038/nature11529

Ahlbeck J, Song L, Chini M, Bitzenhofer SH, Hanganu-Opatz IL. 2018. Glutamatergic drive along the septo-temporal axis of hippocampus boosts prelimbic oscillations in the neonatal mouse. *eLife* **7**:e33158. doi:10.7554/eLife.33158

Basu J, Zaremba JD, Cheung SK, Hitti FL, Zemelman BV, Losonczy A, Siegelbaum SA. 2016. Gating of hippocampal activity, plasticity, and memory by entorhinal cortex long-range inhibition. *Science* **351**. doi:10.1126/science.aaa5694

Bibbig A, Traub RD, Whittington MA. 2002. Long-range synchronization of gamma and beta oscillations and the plasticity of excitatory and inhibitory synapses: a network model. *J Neurophysiol* **88**:1634–1654. doi:10.1152/jn.2002.88.4.1634

Bitzenhofer SH, Ahlbeck J, Hanganu-Opatz IL. 2017a. Methodological Approach for Optogenetic Manipulation of Neonatal Neuronal Networks. *Front Cell Neurosci* **11**:239. doi:10.3389/fncel.2017.00239

Bitzenhofer SH, Ahlbeck J, Wolff A, Wiegert JS, Gee CE, Oertner TG, Hanganu-Opatz IL. 2017b. Layer-specific optogenetic activation of pyramidal neurons causes beta-gamma entrainment of neonatal networks. *Nat Commun* **8**:14563. doi:10.1038/ncomms14563

Bitzenhofer SH, Pöpplau JA, Chini M, Marquardt A, Hanganu-Opatz IL. 2021. A transient developmental increase in prefrontal activity alters network maturation and causes cognitive dysfunction in adult mice. *Neuron* **109**:1350-1364.e6. doi:10.1016/j.neuron.2021.02.011

Bitzenhofer SH, Pöpplau JA, Hanganu-Opatz I. 2020. Gamma activity accelerates during prefrontal development. *eLife* **9**:e56795. doi:10.7554/eLife.56795

620 Brockmann MD, Pöschel B, Cichon N, Hanganu-Opatz IL. 2011. Coupled Oscillations
621   Mediate Directed Interactions between Prefrontal Cortex and Hippocampus of the
622   Neonatal Rat. *Neuron* **71**:332–347. doi:10.1016/j.neuron.2011.05.041

623 Che A, Babij R, Iannone AF, Fetcho RN, Ferrer M, Liston C, Fishell G, De Marco García NV.
624   2018. Layer I Interneurons Sharpen Sensory Maps during Neonatal Development.
625   *Neuron* **99**:98-116.e7. doi:10.1016/j.neuron.2018.06.002

626 Chen G, Rasch MJ, Wang R, Zhang X. 2015. Experience-dependent emergence of beta and
627   gamma band oscillations in the primary visual cortex during the critical period. *Sci*
628   *Rep* **5**:17847. doi:10.1038/srep17847

629 Chini M, Pöpplau JA, Lindemann C, Carol-Perdiguer L, Hnida M, Oberländer V, Xu X,
630   Ahlbeck J, Bitzenhofer SH, Mulert C, Hanganu-Opatz IL. 2020. Resolving and
631   Rescuing Developmental Miswiring in a Mouse Model of Cognitive Impairment.
632   *Neuron* **105**:60-74.e7. doi:10.1016/j.neuron.2019.09.042

633 Cichon NB, Denker M, Grün S, Hanganu-Opatz IL. 2014. Unsupervised classification of
634   neocortical activity patterns in neonatal and pre-juvenile rodents. *Front Neural Circuits*
635   **8**. doi:10.3389/fncir.2014.00050

636 Claudi F, Tyson AL, Petrucco L, Margrie TW, Portugues R, Branco T. 2020. Brainrender: a
637   python-based software for visualizing anatomically registered data. *bioRxiv*
638   2020.02.23.961748. doi:10.1101/2020.02.23.961748

639 David F, Courtiol E, Buonviso N, Fourcaud-Trocmé N. 2015. Competing Mechanisms of
640   Gamma and Beta Oscillations in the Olfactory Bulb Based on Multimodal Inhibition of
641   Mitral Cells Over a Respiratory Cycle. *eNeuro* **2**. doi:10.1523/ENEURO.0018-15.2015

642 Dietz SB, Markopoulos F, Murthy VN. 2011. Postnatal Development of Dendrodendritic
643   Inhibition in the Mammalian Olfactory Bulb. *Front Cell Neurosci* **5**.
644   doi:10.3389/fncel.2011.00010

645 Domnick N-K, Gretenkord S, De Feo V, Sedlacik J, Brockmann MD, Hanganu-Opatz IL.
646   2015. Neonatal hypoxia–ischemia impairs juvenile recognition memory by disrupting
647   the maturation of prefrontal–hippocampal networks. *Exp Neurol* **273**:202–214.
648   doi:10.1016/j.expneurol.2015.08.017

649 Fletcher ML, Smith AM, Best AR, Wilson DA. 2005. High-Frequency Oscillations Are Not
650   Necessary for Simple Olfactory Discriminations in Young Rats. *J Neurosci* **25**:792–
651   798. doi:10.1523/JNEUROSCI.4673-04.2005

652 Fourcaud-Trocmé N, Courtiol E, Buonviso N. 2014. Two distinct olfactory bulb sublaminar
653   networks involved in gamma and beta oscillation generation: a CSD study in the
654   anesthetized rat. *Front Neural Circuits* **8**. doi:10.3389/fncir.2014.00088

655 Gourévitch B, Kay LM, Martin C. 2010. Directional Coupling From the Olfactory Bulb to the
656   Hippocampus During a Go/No-Go Odor Discrimination Task. *J Neurophysiol*
657   **103**:2633–2641. doi:10.1152/jn.01075.2009

658 Gretenkord S, Kostka JK, Hartung H, Watznauer K, Fleck D, Minier-Toribio A, Spehr M,
659   Hanganu-Opatz IL. 2019. Coordinated electrical activity in the olfactory bulb gates the
660   oscillatory entrainment of entorhinal networks in neonatal mice. *PLOS Biol*
661   **17**:e2006994. doi:10.1371/journal.pbio.2006994

662 Hanganu IL, Ben-Ari Y, Khazipov R. 2006. Retinal Waves Trigger Spindle Bursts in the
663   Neonatal Rat Visual Cortex. *J Neurosci* **26**:6728–6736.
664   doi:10.1523/JNEUROSCI.0752-06.2006

665 Hanganu-Opatz IL. 2010. Between molecules and experience: Role of early patterns of
666   coordinated activity for the development of cortical maps and sensory abilities. *Brain*
667   *Res Rev* **64**:160–176. doi:10.1016/j.brainresrev.2010.03.005

668   Hartung H, Brockmann MD, Pöschel B, Feo VD, Hanganu-Opatz IL. 2016a. Thalamic and
669   Entorhinal Network Activity Differently Modulates the Functional Development of
670   Prefrontal–Hippocampal Interactions. *J Neurosci* **36**:3676–3690.
671   doi:10.1523/JNEUROSCI.3232-15.2016
672   Hartung H, Cichon N, De Feo V, Riemann S, Schildt S, Lindemann C, Mulert C, Gogos JA,
673   Hanganu-Opatz IL. 2016b. From Shortage to Surge: A Developmental Switch in
674   Hippocampal–Prefrontal Coupling in a Gene–Environment Model of Neuropsychiatric
675   Disorders. *Cereb Cortex* **26**:4265–4281. doi:10.1093/cercor/bhw274
676   Hoy JL, Niell CM. 2015. Layer-Specific Refinement of Visual Cortex Function after Eye
677   Opening in the Awake Mouse. *J Neurosci* **35**:3370–3383.
678   Igarashi KM, Ieki N, An M, Yamaguchi Y, Nagayama S, Kobayakawa K, Kobayakawa R,
679   Tanifuji M, Sakano H, Chen WR, Mori K. 2012. Parallel Mitral and Tufted Cell
680   Pathways Route Distinct Odor Information to Different Targets in the Olfactory Cortex.
681   *J Neurosci* **32**:7970–7985. doi:10.1523/JNEUROSCI.0154-12.2012
682   Igarashi KM, Lu L, Colgin LL, Moser M-B, Moser EI. 2014. Coordination of entorhinal–
683   hippocampal ensemble activity during associative learning. *Nature* **510**:143–147.
684   doi:10.1038/nature13162
685   Iwasaki S, Sasaki T, Ikegaya Y. 2021. Hippocampal beta oscillations predict mouse object-
686   location associative memory performance. *Hippocampus* **31**:503–511.
687   doi:10.1002/hipo.23311
688   Kay LM. 2014. Chapter 9 - Circuit Oscillations in Odor Perception and Memory In: Barkai E,
689   Wilson DA, editors. Progress in Brain Research, Odor Memory and Perception.
690   Elsevier. pp. 223–251. doi:10.1016/B978-0-444-63350-7.00009-7
691   Khazipov R, Sirota A, Leinekugel X, Holmes GL, Ben-Ari Y, Buzsáki G. 2004. Early motor
692   activity drives spindle bursts in the developing somatosensory cortex. *Nature*
693   **432**:758–761. doi:10.1038/nature03132
694   Kopell N, Ermentrout GB, Whittington MA, Traub RD. 2000. Gamma rhythms and beta
695   rhythms have different synchronization properties. *Proc Natl Acad Sci* **97**:1867–1872.
696   doi:10.1073/pnas.97.4.1867
697   Kopell N, Whittington MA, Kramer MA. 2011. Neuronal assembly dynamics in the beta1
698   frequency range permits short-term memory. *Proc Natl Acad Sci* **108**:3779–3784.
699   doi:10.1073/pnas.1019676108
700   Kostka JK, Gretenkord S, Spehr M, Hanganu-Opatz IL. 2020. Bursting mitral cells time the
701   oscillatory coupling between olfactory bulb and entorhinal networks in neonatal mice.
702   *J Physiol* **598**:5753–5769. doi:10.1113/JP280131
703   Krüger H-S, Brockmann MD, Salamon J, Ittrich H, Hanganu-Opatz IL. 2012. Neonatal
704   hippocampal lesion alters the functional maturation of the prefrontal cortex and the
705   early cognitive development in pre-juvenile rats. *Neurobiol Learn Mem* **97**:470–481.
706   doi:10.1016/j.nlm.2012.04.001
707   Leighton AH, Lohmann C. 2016. The Wiring of Developing Sensory Circuits—From
708   Patterned Spontaneous Activity to Synaptic Plasticity Mechanisms. *Front Neural
709   Circuits* **10**. doi:10.3389/fncir.2016.00071
710   Li Y, Xu J, Liu Y, Zhu J, Liu N, Zeng W, Huang N, Rasch MJ, Jiang H, Gu X, Li X, Luo M, Li
711   C, Teng J, Chen J, Zeng S, Lin L, Zhang X. 2017. A distinct entorhinal cortex to
712   hippocampal CA1 direct circuit for olfactory associative learning. *Nat Neurosci*
713   **20**:559–570. doi:10.1038/nn.4517

714 Logan DW, Brunet LJ, Webb WR, Cutforth T, Ngai J, Stowers L. 2012. Learned recognition
715   of maternal signature odors mediates the first suckling episode in mice. *Curr Biol CB*
716   **22**:1998–2007. doi:10.1016/j.cub.2012.08.041
717 Luskin MB, Price JL. 1983. The topographic organization of associational fibers of the
718   olfactory system in the rat, including centrifugal fibers to the olfactory bulb. *J Comp*
719   *Neurol* **216**:264–291. doi:10.1002/cne.902160305
720 Martin C, Beshel J, Kay LM. 2007. An Olfacto-Hippocampal Network Is Dynamically Involved
721   in Odor-Discrimination Learning. *J Neurophysiol* **98**:2196–2205.
722   doi:10.1152/jn.00524.2007
723 Martin C, Gervais R, Messaoudi B, Ravel N. 2006. Learning-induced oscillatory activities
724   correlated to odour recognition: a network activity. *Eur J Neurosci* **23**:1801–1810.
725   doi:10.1111/j.1460-9568.2006.04711.x
726 Mizuno H, Luo W, Tarusawa E, Saito YM, Sato T, Yoshimura Y, Itohara S, Iwasato T. 2014.
727   NMDAR-regulated dynamics of layer 4 neuronal dendrites during thalamocortical
728   reorganization in neonates. *Neuron* **82**:365–379. doi:10.1016/j.neuron.2014.02.026
729 Neville KR, Haberly LB. 2003. Beta and Gamma Oscillations in the Olfactory System of the
730   Urethane-Anesthetized Rat. *J Neurophysiol* **90**:3921–3930.
731   doi:10.1152/jn.00475.2003
732 Nolte G, Bai O, Wheaton L, Mari Z, Vorbach S, Hallett M. 2004. Identifying true brain
733   interaction from EEG data using the imaginary part of coherency. *Clin Neurophysiol*
734   **115**:2292–2307. doi:10.1016/j.clinph.2004.04.029
735 Osinski BL, Kay LM. 2016. Granule cell excitability regulates gamma and beta oscillations in
736   a model of the olfactory bulb dendrodendritic microcircuit. *J Neurophysiol* **116**:522–
737   539. doi:10.1152/jn.00988.2015
738 Osinski BL, Kim A, Xiao W, Mehta NM, Kay LM. 2018. Pharmacological manipulation of the
739   olfactory bulb modulates beta oscillations: testing model predictions. *J Neurophysiol*
740   **120**:1090–1106. doi:10.1152/jn.00090.2018
741 Ramirez-Villegas JF, Besserve M, Murayama Y, Evrard HC, Oeltermann A, Logothetis NK.
742   2021. Coupling of hippocampal theta and ripples with pontogeniculooccipital waves.
743   *Nature* **589**:96–102. doi:10.1038/s41586-020-2914-4
744 Rangel LM, Rueckemann JW, Riviere PD, Keefe KR, Porter BS, Heimbuch IS, Budlong CH,
745   Eichenbaum H. 2016. Rhythmic coordination of hippocampal neurons during
746   associative memory processing. *eLife* **5**:e09849. doi:10.7554/eLife.09849
747 Ravel N, Chabaud P, Martin C, Gaveau V, Hugues E, Tallon-Baudry C, Bertrand O, Gervais
748   R. 2003. Olfactory learning modifies the expression of odour-induced oscillatory
749   responses in the gamma (60–90 Hz) and beta (15–40 Hz) bands in the rat olfactory
750   bulb. *Eur J Neurosci* **17**:350–358. doi:https://doi.org/10.1046/j.1460-
751   9568.2003.02445.x
752 Richter M, Murtaza N, Scharrenberg R, White SH, Johanns O, Walker S, Yuen RKC,
753   Schwanke B, Bedürftig B, Henis M, Scharf S, Kraus V, Dörk R, Hellmann J,
754   Lindenmaier Z, Ellegood J, Hartung H, Kwan V, Sedlacik J, Fiehler J, Schweizer M,
755   Lerch JP, Hanganu-Opatz IL, Morellini F, Scherer SW, Singh KK, Calderon de Anda
756   F. 2019. Altered TAOK2 activity causes autism-related neurodevelopmental and
757   cognitive abnormalities through RhoA signaling. *Mol Psychiatry* **24**:1329–1350.
758   doi:10.1038/s41380-018-0025-5
759 Rio-Bermudez CD, Blumberg MS. 2018. Active Sleep Promotes Functional Connectivity in
760   Developing Sensorimotor Networks. *BioEssays* **40**:1700234.
761   doi:10.1002/bies.201700234

762 Rossant C, Kadir SN, Goodman DFM, Schulman J, Hunter MLD, Saleem AB, Grosmark A,
763   Belluscio M, Denfield GH, Ecker AS, Tolias AS, Solomon S, Buzsaki G, Carandini M,
764   Harris KD. 2016. Spike sorting for large, dense electrode arrays. *Nat Neurosci*
765   **19**:634–641. doi:10.1038/nn.4268
766 Roth BL. 2016. DREADDs for Neuroscientists. *Neuron* **89**:683–694.
767   doi:10.1016/j.neuron.2016.01.040
768 Schwerdtfeger WK, Buhl EH, Germroth P. 1990. Disynaptic olfactory input to the
769   hippocampus mediated by stellate cells in the entorhinal cortex. *J Comp Neurol*
770   **292**:163–177. doi:https://doi.org/10.1002/cne.902920202
771 Shajarisales N, Janzing D, Shoelkopf B, Besserve M. 2015. Telling cause from effect in
772   deterministic linear dynamical systems. *ArXiv150301299 Cs*.
773 Siapas AG, Lubenov EV, Wilson MA. 2005. Prefrontal Phase Locking to Hippocampal Theta
774   Oscillations. *Neuron* **46**:141–151. doi:10.1016/j.neuron.2005.02.028
775 Spitzer B, Haegens S. 2017. Beyond the Status Quo: A Role for Beta Oscillations in
776   Endogenous Content (Re)Activation. *eNeuro* **4**:ENEURO.0170-17.2017.
777   doi:10.1523/ENEURO.0170-17.2017
778 Stachniak TJ, Ghosh A, Sternson SM. 2014. Chemogenetic synaptic silencing of neural
779   circuits localizes a hypothalamus→midbrain pathway for feeding behavior. *Neuron*
780   **82**:797–808. doi:10.1016/j.neuron.2014.04.008
781 Symanski CA, Bladon JH, Kullberg ET, Jadhav SP. 2021. Rhythmic coordination of
782   hippocampal-prefrontal ensembles for odor-place associative memory and decision
783   making. *bioRxiv* 2020.06.08.140939. doi:10.1101/2020.06.08.140939
784 Thompson KJ, Khajehali E, Bradley SJ, Navarrete JS, Huang XP, Slocum S, Jin J, Liu J,
785   Xiong Y, Olsen RHJ, Diberto JF, Boyt KM, Pina MM, Pati D, Molloy C, Bundgaard C,
786   Sexton PM, Kash TL, Krashes MJ, Christopoulos A, Roth BL, Tobin AB. 2018.
787   DREADD Agonist 21 Is an Effective Agonist for Muscarinic-Based DREADDs in Vitro
788   and in Vivo. *ACS Pharmacol Transl Sci* **1**:61–72. doi:10.1021/acsptsci.8b00012
789 Tort ABL, Komorowski R, Eichenbaum H, Kopell N. 2010. Measuring Phase-Amplitude
790   Coupling Between Neuronal Oscillations of Different Frequencies. *J Neurophysiol*
791   **104**:1195–1210. doi:10.1152/jn.00106.2010
792 Vanderwolf CH, Zibrowski EM. 2001. Pyriform cortex β-waves: odor-specific sensitization
793   following repeated olfactory stimulation. *Brain Res* **892**:301–308. doi:10.1016/S0006-
794   8993(00)03263-7
795 Walz A, Omura M, Mombaerts P. 2006. Development and topography of the lateral olfactory
796   tract in the mouse: Imaging by genetically encoded and injected fluorescent markers.
797   *J Neurobiol* **66**:835–846. doi:https://doi.org/10.1002/neu.20266
798 Wang HC, Bergles DE. 2015. Spontaneous activity in the developing auditory system. *Cell*
799   *Tissue Res* **361**:65–75. doi:10.1007/s00441-014-2007-5
800 Welker WI. 1964. Analysis of Sniffing of the Albino Rat. *Behaviour* **22**:223–244.
801 Wouterlood FG, Nederlof J. 1983. Terminations of olfactory afferents on layer II and III
802   neurons in the entorhinal area: degeneration-Golgi-electron microscopic study in the
803   rat. *Neurosci Lett* **36**:105–110. doi:10.1016/0304-3940(83)90250-1
804 Xu W, Wilson DA. 2012. Odor-evoked activity in the mouse lateral entorhinal cortex.
805   *Neuroscience* **223**:12–20. doi:10.1016/j.neuroscience.2012.07.067
806 Xu X, Song L, Kringel R, Hanganu-Opatz IL. 2021. Developmental decrease of entorhinal
807   gate disrupts prefrontal-hippocampal communication in immune-challenged DISC1
808   knockdown mice. *Res Sq*. doi:10.21203/rs.3.rs-290304/v1

809   Yu Y, Burton SD, Tripathy SJ, Urban NN. 2015. Postnatal development attunes olfactory bulb
810   mitral cells to high-frequency signaling. *J Neurophysiol* **114**:2830–2842.
811   doi:10.1152/jn.00315.2015